

NASA TECHNICAL NOTE



NASA TN D-8069 *ci*

NASA TN D-8069

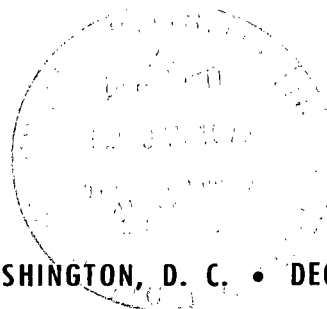


LOAN COPY: RETURN TO  
AFWL TECHNICAL LIBRARY  
KIRTLAND AFB, N. M.

# NONREACTIVE MIXING STUDY OF A SCRAMJET SWEEP-STRUT FUEL INJECTOR

*Charles R. McClinton, Marvin G. Torrence,  
Paul B. Gooderum, and Irene G. Young*

*Langley Research Center  
Hampton, Va. 23665*



NATIONAL AERONAUTICS AND SPACE ADMINISTRATION • WASHINGTON, D. C. • DECEMBER 1975



0133690

1. Report No. <b>NASA TN D-8069</b>		2. Government Accession No.		3. Recipient's Catalog No.	
4. Title and Subtitle <b>NONREACTIVE MIXING STUDY OF A SCRAMJET SWEEP-STRUT FUEL INJECTOR</b>		5. Report Date <b>December 1975</b>		6. Performing Organization Code	
7. Author(s) <b>Charles R. McClinton, Marvin G. Torrence, Paul B. Gooderum, and Irene G. Young</b>		8. Performing Organization Report No. <b>L-10383</b>		10. Work Unit No. <b>505-05-41-01</b>	
9. Performing Organization Name and Address <b>NASA Langley Research Center Hampton, Va. 23665</b>		11. Contract or Grant No.		13. Type of Report and Period Covered <b>Technical Note</b>	
12. Sponsoring Agency Name and Address <b>National Aeronautics and Space Administration Washington, D.C. 20546</b>		14. Sponsoring Agency Code			
15. Supplementary Notes					
16. Abstract  <p>This report presents the results of a cold-mixing investigation performed to supply combustor design information and to determine optimum normal fuel-injector configurations for a general scramjet swept-strut fuel injector. The experimental investigation was made with two swept struts in a closed duct at a Mach number of 4.4 and a nominal ratio of jet mass flow to air mass flow of 0.0295, with helium used to simulate hydrogen fuel. Four injector patterns were evaluated; they represented the range of hole spacing and the ratio of jet dynamic pressure to free-stream dynamic pressure. Helium concentration, pitot pressure, and static pressure in the downstream mixing region were measured to generate the contour plots needed to define the mixing-region flow field and the mixing parameters. Experimental results show that the fuel penetration from the struts was less than the predicted values based on flat-plate data; but the mixing rate was faster and produced a mixing length less than one-half that predicted.</p>					
17. Key Words (Suggested by Author(s)) <b>Air-breathing propulsion Turbulent mixing Nonreactive mixing</b>			18. Distribution Statement <b>Unclassified -- Unlimited</b>  <b>Subject Category 07</b>		
19. Security Classif. (of this report) <b>Unclassified</b>	20. Security Classif. (of this page) <b>Unclassified</b>	21. No. of Pages <b>41</b>	22. Price* <b>\$3.75</b>		

# NONREACTIVE MIXING STUDY OF A SCRAMJET SWEPT-STRUT FUEL INJECTOR

Charles R. McClinton, Marvin G. Torrence, Paul B. Gooderum, and Irene G. Young  
Langley Research Center

## SUMMARY

This report presents the results of a cold-mixing investigation performed to supply combustor design information and to determine optimum normal fuel-injector configurations for a general scramjet swept-strut fuel injector. The experimental investigation was made with two swept struts in a closed duct at a Mach number of 4.4 and a nominal ratio of jet mass flow to air mass flow of 0.0295, with helium used to simulate hydrogen fuel. Four injector patterns were evaluated; they represented the range of hole spacing and the ratio of jet dynamic pressure to free-stream dynamic pressure. Helium concentration, pitot pressure, and static pressure in the downstream mixing region were measured to generate the contour plots needed to define the mixing-region flow field and the mixing parameters. Experimental results show that the fuel penetration from the struts was less than the predicted values based on flat-plate data; but the mixing rate was faster and produced a mixing length less than one-half that predicted.

## INTRODUCTION

Scramjet concepts under study at the Langley Research Center have evolved from basic axisymmetric designs, such as tested under the NASA Hypersonic Research Engine (HRE) Project (see ref. 1), to modular, airframe-integrated designs (see refs. 2 and 3). These latter scramjets feature rectangular combustors with relatively small internal surface area, and thus lower cooling requirements, and use portions of the airframe for inlet compression and nozzle expansion. Also, a significant fraction of the inlet compression is accomplished by swept fuel-injector struts.

Preliminary analyses of scramjet combustor concepts have generally been based on data obtained from flat-plate cold-mixing studies (refs. 4 to 9). The flat-plate geometry was selected to minimize flow nonuniformities so that injector variables could be investigated. These test results have been used to simulate the penetration and mixing in annular combustors, such as the HRE. Mixing efficiencies calculated from these test data have been shown (ref. 2) to accurately represent the combustion rates experienced in similar hot-mixing combustion studies. Some cold-mixing studies have been made with swept-strut fuel injectors (ref. 10). Mixing results for strut injector tests are expected to be strongly dependent on

---

the particular strut geometry and resulting airflow conditions at the injector station and in the downstream mixing region. The effect of these airflow conditions can be observed by comparison of flat-plate results with the strut injection results.

As discussed in reference 2, fuel-injector struts can be used for parallel injection at low combustor-air velocity and for normal injection at high velocity. At high velocity, or high free-stream Mach numbers, normal injection is required to maintain a relatively short combustor for engine weight and heating optimization; but at lower combustor velocity, parallel injection can be used to reduce mixing losses inherent with normal mixing and to spread the heat release over the combustor length. This report looks only at the former case.

The present work was performed: to study the fuel-air mixing on a basic swept strut having the general characteristics of that to be used in the modular, airframe-integrated scramjet; to determine the appropriate injector array or configuration; and to compare the mixing with empirical predictions based on flat-plate mixing results. Primary emphasis is placed on reducing or minimizing the mixing length because chemical kinetics considerations have shown that scramjet combustion is largely mixing dependent (ref. 11).

All tests were run using two adjacent struts with injection from both sides of each strut. Tunnel sidewalls were located to either side of the struts at half the spacing between the two struts. No injection from the wall was employed, and the mixing studied was that initiated between the struts. The total flow between struts and sidewalls has the same bulk concentration as the flow between the struts and serves to reduce the end effects. Injector design variables studied are ratio of jet dynamic pressure to free-stream dynamic pressure, jet lateral spacing, number of jet orifices, and jet diameter. All tests were run at a free-stream tunnel Mach number of 4.4, stagnation temperature of 300 K, and stagnation pressure of 3.896 MPa. The free-stream Reynolds number, based on these test conditions and a strut-gap dimension of 2.30 cm, was  $3.327 \times 10^6$ . Helium gas was used to simulate hydrogen fuel, and the fuel injectors were operated at sonic velocity in each configuration. Results presented in reference 9 show that both the penetration and the mixing rate of hydrogen can be closely simulated by helium. Data measured include mixing-region surveys of pitot pressure, static pressure, and gas composition.

## SYMBOLS

A,B,C	coefficients used in equation (2)
$C_D$	jet discharge coefficient (average of all jets in configuration)
d	jet orifice diameter, cm

G	distance of gap between adjacent strut shoulders, 2.30 cm
L	mixing length to $\eta_m = 0.95$ , cm
M	Mach number
$\dot{m}$	mass flow rate, kg/sec
N	total number of helium jets
P	jet penetration (vertical distance from injector to $\alpha_{\text{He}} = 0$ ), cm
p	pressure, Pa
q	dynamic pressure, Pa
$q_r$	ratio of jet dynamic pressure to inviscid undisturbed (no injection) air dynamic pressure at jet station
R	Reynolds number (based on free-stream flow conditions and strut gap G)
s	jet spacing, cm
V	velocity, m/sec
x	streamwise coordinate (see fig. 4), cm
y	lateral coordinate (see fig. 4), cm
$Z_1$	edge of streamtube at jet station (see fig. 2), cm
$Z'$	edge of streamtube at survey station (see fig. 2), cm
z	vertical coordinate (see fig. 4), cm
$\alpha$	injected-gas mass fraction
$\delta$	boundary-layer thickness, cm

$\delta^*$	boundary-layer displacement thickness, cm
$\eta_m$	mixing efficiency
$\Lambda$	strut sweep angle, $48^\circ$
$\rho$	density, $\text{kg/m}^3$
$\phi$	simulated equivalence ratio, $(\dot{m}_{\text{He}}/\dot{m}_{\text{air}})/0.0295$

Subscripts:

air	air
He	helium gas
j	jet condition
max	maximum value in mixing region
t	stagnation conditions
w	tunnel-wall condition
$\infty$	free-stream tunnel condition

## TEST-CONFIGURATION PHILOSOPHY

A sketch of the swept-strut model is presented in figure 1. Two identical hollow struts were used throughout this investigation; the injector pattern on the struts was the test variable. Details of injector geometry are discussed in the subsequent section “Test Apparatus and Procedures.” The remainder of this section considers the philosophy used in selecting the injector geometry and test conditions.

### Strut Selection

The strut geometry used in this investigation was a simple diamond cross section with wedge and sweep angles similar to current modular scramjet concepts (i.e., ref. 2). The strut geometry was selected to produce strut leading-edge shock-wave cancellation on the opposite

strut shoulders at the design free-stream conditions. Shock and expansion wave locations were calculated for both design and off-design conditions by an updated version of the swept shock-wave program described in reference 3.

### Injector Selection

With tunnel size, strut geometry, and tunnel free-stream conditions specified, preliminary fuel-injector design parameters (i.e., jet location, injection angle, dynamic pressure ratio  $q_r$ , jet spacing, and jet diameter) were determined from flat-plate mixing results (see refs. 4 to 9). Important characteristics considered in injector selection include: good fuel distribution, penetration and spreading, rapid mixing, and fuel equivalence ratio. All jets are sonic to simplify fuel delivery system with regard to determining mass flow rates and to maintain steady flows unaffected by combustor conditions. Supersonic injection adds little to the penetration distance, so it is not currently anticipated as a test parameter of interest.

Fuel injectors are located directly downstream of the strut shoulder near the minimum channel width where required penetration is smallest. Normal or angular injection is preferred to coaxial injection at high combustor Mach numbers because faster initial mixing rates are obtained. Reference 4 showed that better performance (penetration and mixing rate) was obtained by angular (downstream) injection; however, for these tests only normal injection is used because of the large quantity of comparable flat-plate data.

Jet-diameter sizing is based on the penetration results (see ref. 6) of single normal jets on a flat plate. To obtain a good fuel distribution, an opposite staggered jet pattern is used, as shown in figure 2(a). Considering the shape of the superimposed single-jet mixing regions shown in this figure, a jet of sufficient size is selected so that the point of half maximum concentration (see fig. 2(b)) is located on the center line between the struts. Thereby, the lower concentration in the outer edge of one jet mixing region is reinforced by the low concentrations in the outer edge of the mixing regions from the two adjacent jets on the opposite wall. For basic flat-plate type normal injection, the injectant obtains most of its penetration at the jet station. In the downstream region, the edge expands by turbulent diffusion, but the bulk penetration remains nearly constant. For the present injection process, the mainstream flow expands downstream of the injectors, complicating the penetration comparison to the flat-plate configurations. A method suggested in reference 6 to compare penetration for these two cases is not affected by these geometry differences. The quantity of air in the flat-plate single-jet mixing region under  $\frac{1}{2}\alpha_{\max}$  (see fig. 2(b)) is used to determine the size of the undisturbed airstream tube at the jet station used for mixing. The height  $Z_1$  of this stream-tube corresponds to  $\frac{1}{2}G$  in the strut model. Values of  $Z_1/d$  from reference 6 suggest that for the current tests  $3 \leq \frac{G}{d} \leq 5$  is appropriate for good fuel penetration. A range of jet diameters is considered because, in addition to controlling fuel penetration, the jet diameter

must be correlated, through the continuity equation, with jet spacing and dynamic pressure to assure that the desired equivalence ratio  $\phi$  is maintained. Therefore, the range of  $G/d$  is a variable in the following equation derived from continuity:

$$\phi = \frac{\left(\frac{\pi C_D}{4}\right) q_r}{0.0295 \left(\frac{1}{2}\right) \left(\frac{s}{d}\right) \left(\frac{G}{d}\right) \left(\frac{V_j}{V_\infty}\right)} \quad (1)$$

Before solving equation (1), values must be selected for the dynamic pressure ratio  $q_r$  and the ratio of jet spacing to orifice diameter  $s/d$ .

Selecting values for  $q_r$  and  $s/d$  is accomplished using the mixing efficiency parameter  $\eta_m$  (see ref. 7). At any downstream station,  $\eta_m$  is defined as the fraction of the injected fuel that would burn if complete chemical reaction occurred without further mixing. The following mixing efficiency correlation was developed from data presented in reference 7 and unpublished flat-plate results:

$$\eta_m = A \left(\frac{x}{d}\right)^B (q_r)^C \quad (2)$$

where

$$A = 0.109 + 0.0301 \left(\frac{s}{d}\right)$$

$$B = 0.271 - 0.00976 \left(\frac{s}{d}\right)$$

$$C = -0.534 + 0.0347 \left(\frac{s}{d}\right)$$

Equation (2) is a useful tool in relating cold- and hot-mixing studies. In most scramjet applications, supersonic combustion is mixing dependent; that is, fuel mixing is the controlling part of the combustion processes. For this type of combustion, the mixing efficiency parameter obtained in cold tests has been shown (ref. 2) to be nearly the same as the combustion efficiency parameter measured in hot tests.

Equations (1) and (2) were solved assuming  $C_D = 0.75$  and substituting theoretical values of  $\phi = 1.0$  and  $\frac{V_j}{V_\infty} = 1.33$  to produce the predicted mixing length to  $\eta_m = 0.95$  as a function of jet diameter, jet spacing, and ratio of jet dynamic pressure to free-stream dynamic pressure shown in figure 3. The solid lines in this figure represent constant jet diameter solutions, and the dashed lines represent constant dynamic pressure. Three limits must be imposed on actual geometry selection. First, since the jet is sonic, the jet static



pressure must be higher than the effective back pressure in the separated region surrounding the jet; for this test, the smallest value of  $q_T$  which would produce sonic flow was determined experimentally and found to be  $q_T = 0.5$ . Second, the spacing between adjacent jets must be less than 8 to 9 diameters to insure merging of adjacent jets at far downstream stations; the horizontal crosshatch region at  $s/d = 8.5$  represents this limit. The last limit  $G/d$  was discussed previously in this section. This limit is represented by the shaded area. Considering these three limits, the flat-plate prediction indicates that optimum injector design incorporated the lowest dynamic pressure ratio which produces sonic flow ( $q_T = 0.5$ ) and a value of  $G/d < 4.2$  with jet spacing less than 4 diameters.

### Hydrogen Simulation

Because of hazards involved in testing with large flow rates of hydrogen, helium was chosen as a substitute gas. Two factors were considered when selecting appropriate test conditions using helium to simulate hydrogen. Previous cold-mixing studies, reference 9, have shown that the penetration and mixing rate of hydrogen and helium are nearly the same when the dynamic pressure ratios are the same. Also, mixing theories are dependent on mass ratios, not mole ratios as are kinetic theories.

Results with helium injection represent the mixing results expected for hydrogen injected at the same dynamic pressure ratio  $q_T$  and mass flow ratio  $\dot{m}_j/\dot{m}_{air}$  from jets at the specified spacings  $s/d$ . When applying the present results to an actual combustor with hydrogen fuel, a larger diameter jet will be used.

### TEST APPARATUS AND PROCEDURES

Tests were conducted in a 7.62-cm by 15.24-cm Mach 4.4 blowdown wind tunnel. Two identical hollow struts were mounted vertically (see fig. 1) in the test section by two end plates flush mounted in the tunnel top and bottom walls. Both end plates anchored the struts and, in addition, the top plate served as a cap for the simulated fuel settling chamber. The tunnel cross section in figure 1 illustrates the strut top end plate fit to both the top of the tunnel (forming the fuel settling chamber) and the two struts. Strut details are shown in the strut cross section. The strut design used was symmetrical with  $4^\circ$  half-wedge angles (in the plane of the free-stream flow velocity) for leading and trailing edges and a sweep angle  $\Lambda$  of  $48^\circ$ . Each strut has sufficient internal fuel flow area so that the maximum fuel Mach number is 0.30, producing a 1.5-percent fuel pressure loss through the strut from the settling chamber pressure. For all configurations tested, fuel injectors were centered 1.28 cm downstream of the strut shoulder.

The coordinate system (see fig. 4) is a floating origin rectangular system referenced to the  $48^\circ$  swept plane with  $x$  measured downstream from the strut shoulder,  $y$  measured

across the tunnel from the center line between the struts, and  $z$  measured from the tunnel floor.

Tunnel and strut instrumentation consist of various static pressure orifices and detectors for total temperature and pressure measurements of the free-stream and jet flows. Tunnel static pressure orifices (0.10-cm diam) are depicted in figure 4. One row of static orifices runs along the test section and diffuser sidewall center line. In the vicinity of the struts these orifices are spaced at 1.28-cm intervals. The other row of orifices is on the tunnel sidewall at  $x/G = 0$ , parallel to the strut shoulder. In addition, static orifices are located in the strut base plate between the struts. Static pressure measurements on the struts were made using solid dummy struts with pressure orifices located on both sides along the line  $z = 7.62$  cm. Tunnel total pressure and temperature were measured in the 0.406-m diameter pipe section ahead of the tunnel settling chamber, and the jet total pressure and temperature were measured in the helium settling chamber. As a check, the jet total pressure was also measured in the bottom of one strut.

Four injector geometry configurations were selected for testing. A summary of geometry and test conditions for these configurations is presented in table I. Free-stream conditions are the same for all tests. Free-stream Reynolds numbers presented are based on the strut gap (2.30 cm). The only variables between the first three configurations are jet spacing and dynamic pressure. Configuration IV has, in addition, a larger jet diameter. Configuration I, designed to operate at  $q_r = 2$ , was run at  $q_r = 1.4$ .

Helium was supplied from a trailer to the fuel settling chamber by the supply system shown in figure 5. The pressure regulators were preset so that the helium flow was controlled by actuating the ball valve.

A seven-probe pitot pressure and gas sampling rake and a seven-probe static pressure rake were used to survey the helium-air mixing region. Details of these are shown in figure 6. Both rakes have the same sweep angle as the struts ( $48^\circ$ ); so all probe tips are at a constant  $x$ -location. Each rake is moved across the tunnel ( $\pm y$ -direction). The pitot and gas sampling probe is an internal expansion type with a tip inside diameter of 0.3 mm expanding to a tube inside diameter of 1.0 mm. Both calculations and actual measurements indicate no flow field interference exists between adjacent pitot probes within the range of flow conditions measured. But, this is not the case for the static probe rake using conventional static probes. Regular static probes with tip-to-orifice lengths of greater than 10 diameters produced shock-wave interference between adjacent probes. Also, in the confined region between the struts, the probe tip shock reflection off the struts affected the measured pressure. These problems led to the development of the static probe design shown in figure 6. These probes, developed by Pinckney (ref. 12), are shorter from tip to static orifices to help alleviate tip shock interference. Also, tests have shown these probes are less susceptible to errors from misalignment.

Each static probe was individually calibrated in the uniform Mach 4.4 free stream to assure accuracy of measurements.

The pitot probe is also used to collect gas samples by the gas sampling system shown in figure 5. Each probe is attached by a short length of tubing and a solenoid valve to a sample collection bottle. The transducers to measure pitot pressure are connected into the line between the pitot probes and sample-bottle control valve. The contents of the sample bottles are analyzed on a process gas chromatograph for helium, nitrogen, and oxygen volume fractions.

The same general procedure is followed for both pitot and static probe surveys. For each survey, the tunnel flow is established, and a no-injection data scan is taken before helium is injected. Then the injectant flow is established by actuating the helium ball valve. Data are taken as soon as the flow is steady (about 2 sec). The first data taken are the settling-chamber total pressure and survey pitot pressures. Once these pressures have been recorded, the gas samples are obtained while the remainder of the data is recorded. To take gas samples, the evacuated sample bottles (open to the vacuum reservoir) are open to the pitot probes. After 2- or 3-sec purge of the pitot probe connecting tubing and bottles, the downstream solenoid valves (fig. 5) are closed and the bottles are allowed to fill for 7 to 10 sec before the upstream solenoid valves are closed. This procedure produced good repeatability of gas-sampling results.

## RESULTS AND DISCUSSION

### Tunnel Calibration

Results of the tunnel Mach number calibration are presented in figures 7 and 8. Figure 7 shows the longitudinal variation of Mach number along the tunnel sidewall as determined from measured wall static pressures and tunnel total pressures.

Transverse pitot and static surveys were taken at  $x/G = 1.91$ , and the resulting Mach number profiles are presented in figure 8. During these surveys, a blank plate was used to cover the helium settling chamber, but the lower strut and end-plate cavity was not filled because it was further downstream and therefore was not expected to influence the calibrations. Consequently, the resulting profiles show flow uniformity down to a value of  $z/G < 2.0$ . Below this value, the flow is affected by combined disturbances from the tunnel boundary layer and from the step produced by the strut end-plate cavity.

### Strut Flow Field

Solid dummy struts with static-pressure instrumentation were installed next, and the resulting flow field was surveyed with the pitot and static rake to check the predicted strut

flow field. Predicted tunnel-wall and strut boundary-layer displacement thickness and shock diagram are presented in figure 9, along with nondimensionalized theoretical and measured tunnel-wall and strut static pressures. The outer passage wall and strut pressures are shown above the airflow shock diagram, and the center passage (between struts) pressure is shown below. These experimental data points substantiate the inviscid prediction method (boundary-layer displacement thickness corrected). Boundary-layer spreading of the shock-induced pressure rise is about as expected (see ref. 13). Inviscid stream conditions in the numbered bays on the diagram are tabulated in the upper left-hand corner of figure 9. The jet, located about 1/3 gap downstream of the strut shoulder, penetrates through the shoulder generated expansion fan and the reflected leading-edge shock wave and into bay ②. Because the penetration distance at this location is not known, the airflow conditions in bay ② are used to represent the airflow at the jet station. In addition to the flow turbulence caused by the shock wave and expansion fan, the emerging jet is also subjected to flow vorticity caused by the swept edges of the strut and the resulting three-dimensional flow field. None of these effects was present in the referenced flat-plate results.

Transverse Mach number profiles at several downstream stations (without helium injection), calculated from the pitot and static pressure survey data, are presented in figure 10. Figure 10(a) compares profiles at constant height ( $z/G$ ) at various downstream stations. These profiles indicate a region of low Mach number wake flow directly behind the struts ( $x/G = 5.0$ ) and a relatively uniform high Mach number flow in the center and side passages. Farther downstream, the wake section of the profile diffuses across the entire flow, with the resulting flattening of the entire profile. Figure 10(b) compares profiles at a fixed downstream station ( $x/G = 6.0$ ) for various values of  $z/G$ . These profiles indicate the strut end effects (lower Mach number for low  $z/G$ ) caused by the strut induced downflow being compressed against the tunnel floor. Surveys above  $z/G = 3.32$  were unaffected and similar to  $z/G = 3.32$ . Because of these end effects, no data other than Mach number distribution are presented for  $x/G < 2.22$ .

#### Jet Flow and Mixing-Region Surveys

Jet discharge coefficients were determined by a mass flow balance between the jets and a venturi meter in the helium supply line. Measured values of jet discharge coefficients for configurations I, II, III, and IV are 0.93, 0.86, 0.61, and 0.71, respectively. Each jet had the same shape, and none of the measured operating discharge coefficients were dependent on dynamic pressure ratio. Therefore, the variation of discharge coefficient is believed associated with the strut internal flow interference between adjacent and opposite jets. The discharge coefficients for configurations II, III, and IV, where such interference is most likely to occur, are accurately represented by

$$C_D = 0.37 \left( \frac{s}{d} \right)^{0.44} \quad (3)$$

Values of  $C_D$  calculated from equation (3) are 1.12, 0.83, 0.61, and 0.71 for configurations I, II, III, and IV, respectively.

The injector geometry and test conditions were selected to produce a bulk helium-to-air mass flow ratio of 0.0295. Two factors caused a variation in the mass flow ratio. First, the assumed value of  $C_D = 0.75$  was not correct; second, configuration I could not be operated at the design value of  $q_T = 2.0$  because the tunnel choked, apparently as a result of the jets separating the tunnel-wall boundary layer. The actual values of the helium-to-air mass flow ratio for configurations I, II, III, and IV are 0.0258, 0.0401, 0.0298, and 0.0360, respectively.

The helium-air mixing region was surveyed at  $x/G = 5.0, 7.2, 11.6,$  and  $22.7$ . A minimum data point grid was chosen, shown in figure 11, which allowed cross plotting in both  $y$  and  $z$  directions with a minimum number of runs. Figure 12 is the tunnel cross section normal to the free-stream flow direction. All points shown are at constant  $x/G$ . The vertical dashed lines depict the lateral position of the struts upstream of the measuring station. Pitot pressure, static pressure, and gas samples were obtained at each point on the grid, and because of the rapid data turn-around, additional points on the constant  $z$  surveys could be added to supplement points in regions of steep or uncertain concentration gradients. The survey data were reduced by a computer program to obtain point values of helium mass fraction, helium mass flow rate, and air mass flow rate, which are cross plotted to produce the desired mixing-region flow-field contours presented in figures 12 to 17.

Helium mass-fraction contours produced by the four injector configurations are presented in figures 12 to 15 at each of the four downstream stations. These contour plots represent the helium distribution measured in a plane which is swept relative to the free stream (swept coordinate system) and presented in the  $yz$ -plane upstream. Each line in the contour plots represents a constant value of helium mass fraction, with the maximum value depicting the center of a jet mixing region. The vertical dashed lines and solid elliptical symbols on each contour plot represent the strut and jet locations, respectively. Individual jet mixing regions are easily discernible for most of the contours, and the regions spread with downstream distance as expected. Configuration I contours (fig. 12) do not merge until after the  $x/G = 11.6$  survey station. For the other configurations, merging is more rapid. Configuration III exhibits very rapid merging between adjacent jet mixing regions but slow merging between regions from opposing struts. Configurations II and IV exhibit a more even merging between adjacent and opposing jet mixing regions. The location of the mixing regions relative to the jet at the four locations gives an indication of the flow turbulence downstream of the swept fuel-injector struts. The struts produce, in addition to a three-dimensional shock expansion flow system, a down turning of the entire flow so that behind the shocks the lower part of the flow is compressed. These contour plots all show an upward shift in the mixing region at the  $x/G = 11.6$  station, apparently caused by the upward redistribution of the flow. The fuel penetration and the decay of the maximum concentration (mixing rate) are obtained from these figures and are discussed in detail in the following sections.

Typical helium and air mass-flow-rate contours are presented in figures 16 and 17, respectively. These contours are integrated to determine helium and airflow rates necessary to calculate both the total measured helium flow and the mixing efficiency  $\eta_m$  at each survey station.

### Fuel Penetration

Fuel penetration is not an easily or clearly defined parameter in confined mixing tests. Penetration is generally defined by the displacement of the outer edge of the mixing region  $P/d$ , but for a confined flow such as this the outer edge of the mixing region is obscured once the opposite jets merge. Penetration has also been defined as the displacement of the point of maximum concentration, but the location of the point of maximum concentration is strongly dependent on the flow-field geometry and the resulting mixing rates and direction. This strong dependence rules out comparison between flat-plate and strut data using this penetration parameter. The few contours which do show the outer edge of the mixing region are used to produce the penetration results shown in figure 18. Also shown, for reference only, is penetration to the point of maximum concentration.

Increasing the dynamic pressure ratio from 0.5 (configuration III) to 1.4 (configuration I) more than doubles the penetration; increasing jet diameter also produces the expected directly proportional increase in penetration as shown by configurations III and IV (see table II). All strut penetration values are smaller than flat-plate values. Results presented in reference 6 were obtained using hydrogen, but reference 9 showed that there is negligible difference in penetration between hydrogen and helium when the dynamic pressure ratio is constant. In the comparison shown in table II, the present penetration is measured at  $x/G \approx 5.0$  ( $x/d = 18$  for configurations I, II, and III;  $x/d = 12.8$  for configuration IV), and the flat-plate penetration is determined by

$$\frac{P}{d} = 3.87(q_r)^{0.3} \left(\frac{x}{d}\right)^{0.143} \quad (4)$$

which is a correlation presented in reference 6 for single-jet data and is used in reference 7 for other jet spacings. Reference 7 showed that jet spacing has no effect on penetration for injection from a flat plate, but jet diameter and dynamic pressure ratio have the expected effect on the penetration. The values of penetration  $P/d$  shown in table II for configurations III and IV indicate that  $P/d$  is independent of jet diameter. The effect of dynamic pressure on penetration is much greater than that of flat-plate mixing. Increasing the dynamic pressure ratio from 0.5 (configuration III) to 1.4 (configuration I) more than doubles the penetration while the flat-plate value of penetration is increased by 30 percent.

The poor penetration observed in these tests can be attributed to one or more of the following factors: (1) Increased back pressure at jet station caused by the jet-induced

aerodynamic contraction, (2) thin boundary layer ( $\delta/d < 0.5$ ) on the struts, (3) shock wave and expansion-fan jet interference, and (4) vorticity generated by the swept edges of the strut.

Additional study in the initial mixing region is required to pinpoint the factors reducing the penetration. Similar penetration results (unpublished) have recently been obtained in simulated strut combustion studies in a combustion heater facility. These tests used wall injection behind a rearward facing step with orifice spacing, dynamic pressure ratio, and measured penetration matching the present test configurations and data.

### Mixing Rate

Decay of the maximum jet concentration ( $\alpha_{\text{He,max}}$ ) has been used extensively as a measure of the rate of mixing. Although the mixing efficiency  $\eta_m$  is a more useful parameter in discussing fuel mixing rates, both  $\alpha_{\text{He,max}}$  and  $\eta_m$  are used herein because some earlier results, as presented, cannot be converted to  $\eta_m$ . Values of maximum concentration decay measured during flat-plate mixing studies are presented separately in figure 19(a) and are compared with the four injector configurations in figures 19(b) to 19(d). Solid lines in figure 19(a) represent the decay of maximum concentration for a single jet (ref. 6) and multiple jets with  $s/d = 12.5$  (ref. 7); dashed lines represent the decay of the maximum concentration for multiple jet studies with  $s/d = 6.25$  (ref. 7). Figure 19(a) illustrates the effect of dynamic pressure and jet spacing on decay of the maximum concentration. For both spacings, faster mixing (i.e., smaller maximum concentration) is observed for lower values of  $q_r$ . For each of the three dynamic pressure ratios shown, the closely spaced jets ( $s/d = 6.25$ ) tend to mix faster initially but at a slower rate farther downstream than the single jet. This characteristic is believed to result from the initial increased turbulence, particularly from the jet-induced shock-wave interference with the adjacent closely spaced jets; and then farther downstream the jet merging becomes predominant, restricting the mixing rate.

Maximum concentration decay for configuration I is presented in figure 19(b) with the flat-plate results for the same jet spacing (12.5) and dynamic pressure ratio (1.5). The experimental results shown in figure 19 have been adjusted to a bulk value of  $\dot{m}_{\text{He}}/\dot{m}_{\text{air}} = 0.0295$ . The rate of decay with  $x/G$  is about the same as the comparative flat-plate case shown, but the initial helium concentration is lower. This faster mixing is believed to result from the increased turbulence typical of the strut flow field as compared with flat-plate flow.

The maximum concentration for configuration II, presented in figure 19(c), shows a slightly faster rate of decay than the similar flat-plate case ( $s/d = 6.25$ ;  $q_r = 1.0$ ), but the initial value is higher. Although this rate of decay is greater than the flat-plate decay rate, it is not as rapid as expected, considering the increased turbulence caused by the strut flow field.

The maximum concentration for configurations III and IV, presented in figure 19(d), decays at a faster rate and has a slightly lower initial value than configuration II. Although

there is no comparable flat-plate data at  $q_r = 0.5$  and  $s/d = 3.13$  or  $4.42$ , extrapolations of results at  $q_r = 0.5$  and  $s/d = 12.5$  are shown as dashed lines in figure 19(d). These extrapolated curves exhibit fast initial mixing and slow downstream mixing. Both configurations III and IV have slower initial mixing but faster downstream mixing than predicted. These results suggest that the jet mixing is retarded in the initial interaction region at the jet, but the increased turbulence in the downstream region accelerates the mixing. The retarded initial mixing would be one result from the small penetration observed in figure 18.

### Mixing Efficiency

Mixing efficiency is defined in reference 7 as that fraction of the fuel that would burn if complete chemical reaction occurred without additional mixing. For these tests, the same definition of  $\eta_m$  is used, except helium mass flow replaces fuel. Mixing efficiency  $\eta_m$  is determined from integrations of the helium and air mass-flow-rate contours. Bulk helium in excess of a local mass fraction of 0.0295,  $\dot{m}_{\text{He,excess}}$ , is determined from integrating both  $\dot{m}_{\text{He},\phi}$  and  $\dot{m}_{\text{air},\phi}$  within the contour  $\phi = 1.0$ , where

$$\dot{m}_{\text{He,excess}} = \dot{m}_{\text{He},\phi} - 0.0295\dot{m}_{\text{air},\phi} \quad (5)$$

This bulk excess helium is used, along with the total measured helium,  $\dot{m}_{\text{He,total}}$ , to define the mixing efficiency

$$\eta_m = \frac{\dot{m}_{\text{He,total}} - \dot{m}_{\text{He,excess}}}{\dot{m}_{\text{He,total}}} \quad (6)$$

In figure 20 experimental mixing efficiency is compared to the values obtained from flat-plate predictions. The predictions, based on equation (2), are represented by the solid lines and the present data, by symbols. Data-point fairings are represented by the dashed curves. Mixing is assumed complete when  $\eta_m$  reaches 0.95. Flat-plate predictions suggest that the mixing length for configuration I would be shortest, configurations III and IV somewhat longer, and configuration II the longest. This trend is observed in the data. As discussed earlier, configuration I behaves as a single jet (i.e., the rate of mixing is not restricted by the downstream merging with adjacent jet mixing region). Thus, the mixing length is considerably shorter than all other configurations. This mixing length is unattainable in a real combustor design where a uniform fuel distribution is required.

Configurations III and IV were chosen as the optimum injector geometries for minimum combustor length with a uniform fuel distribution. Both have nearly the same predicted mixing lengths, but the mixing length measured for configuration III is about 18 percent shorter



than that of configuration IV. However, as discussed previously, configuration IV has better fuel distribution.

The exact nature of the observed increased mixing rate for all four configurations, as compared with the flat-plate prediction, cannot be determined from test results. The increase is assumed to result primarily from the increased turbulence produced by the swept struts and the initial interaction between adjacent jet flow fields. In the downstream region ( $x/G \geq 10$ ) the present results exhibit faster mixing with downstream distance than the flat-plate results. This trend illustrates increased turbulence in the flow.

## CONCLUDING REMARKS

In order to provide supersonic mixing data for a scramjet module configuration which is under study at Langley Research Center, an experimental investigation was conducted utilizing swept fuel-injector struts which, in the scramjet module concept, also provide a part of the inlet aerodynamic compression. The objective of this investigation was to achieve good fuel-air mixing performance for a scramjet combustor featuring fuel injection normal to the local flow from fuel-injector holes of proper size and spacing in the swept struts. Four fuel-injector-hole configurations were designed, based on flat-plate fuel-injection data, to inject ambient temperature helium (simulation for hydrogen fuel) just downstream of the shoulder (maximum width) of two adjacent struts. All four configurations were tested with a test section Mach number ahead of the struts of 4.4, an airstream total temperature of 300 K, and the fuel-injector holes operating sonically. The mixing region was surveyed at four stations from 5 to 22.7 strut gaps downstream of the strut shoulder, and sidewall static pressure measurements were taken.

Fuel penetration was much less than predicted by flat-plate correlations but does agree with recent unpublished combustion test results. Lateral merging of adjacent jets was about as expected. For all configurations, mixing efficiency results show that the mixing rate is faster and the mixing lengths are shorter than predicted by flat-plate correlations.

These results show that the best fuel-injector array for minimum combustor length with relatively uniform fuel-air distribution incorporates large jets with relatively small jet lateral spacing (less than 4.5 jet diameters) operating at the minimum dynamic pressures which produce sonic flow. Two configurations were tested which satisfy these requirements with the following geometry and flow conditions: jet diameters of 0.64 cm and 0.91 cm; jet lateral spacings of 3.13 and 4.40 jet diameters, respectively; and dynamic pressure ratio of 0.5 with sonic flow in the fuel-injection orifices. Neither configuration produced large enough penetration to reach the center line of the combustor at the trailing-edge station of the injection struts, but the turbulent mixing in the downstream flow rapidly diffused the helium across the

combustor. Both configurations exhibit rapid mixing with mixing lengths on the order of 20 strut gaps.

Langley Research Center  
National Aeronautics and Space Administration  
Hampton, Va. 23665  
November 4, 1975

## REFERENCES

1. Staff of Langley Research Center and AiResearch Manufacturing Co., The Garrett Corp.: Hypersonic Research Engine Project Technological Status 1971. NASA TM X-2572, 1972.
2. Henry, John R.; and Anderson, Griffin Y.: Design Considerations for the Airframe-Integrated Scramjet. NASA TM X-2895, 1973.
3. Trexler, Carl Arthur: An Experimental Investigation of the Forebody of a Hypersonic Inlet Model and a Comparison With Theory. M. S. Thesis, Virginia Polytech. Inst. & State Univ., Apr. 1971.
4. McClinton, Charles R.: The Effect of Injection Angle on the Interaction Between Sonic Secondary Jets and a Supersonic Free Stream. NASA TN D-6669, 1972.
5. McClinton, Charles R.: Effect of Ratio of Wall Boundary-Layer Thickness to Jet Diameter on Mixing of a Normal Hydrogen Jet in a Supersonic Stream. NASA TM X-3030, 1974.
6. Rogers, R. Clayton: A Study of the Mixing of Hydrogen Injected Normal to a Supersonic Airstream. NASA TN D-6114, 1971.
7. Rogers, R. Clayton: Mixing of Hydrogen Injected From Multiple Injectors Normal to a Supersonic Airstream. NASA TN D-6476, 1971.
8. Torrence, Marvin G.: Concentration Measurements of an Injected Gas in a Supersonic Stream. NASA TN D-3860, 1967.
9. Torrence, Marvin G.: Effect of Injectant Molecular Weight on Mixing of a Normal Jet in a Mach 4 Airstream. NASA TN D-6061, 1971.
10. Povinelli, Louis A.: Aerodynamic Drag and Fuel Spreading Measurements in a Simulated Scramjet Combustion Module. NASA TN D-7674, 1974.
11. Eng. Staff, AiResearch Manufacturing Co.: Hypersonic Research Engine Project — Phase II. Chemical Kinetics Study for a Supersonic Combustor Model. NASA CR-66959, 1970.
12. Pinckney, S. Z.: An Improved Static Probe Design. AIAA J., vol. 12, no. 4, Apr. 1974, pp. 562-564.
13. Pinckney, S. Z.: Semiempirical Method for Predicting Effects of Incident-Reflecting Shocks on the Turbulent Boundary Layer. NASA TN D-3029, 1965.

TABLE I.- TEST CONDITIONS FOR FOUR INJECTOR CONFIGURATIONS

Configuration	$M_j$	s, cm	d, cm	s/d	$q_r$	$p_{t,j}$ , MPa	$M_\infty$	$p_{t,\infty}$ , MPa	R	G/d	N	$\phi$
I	1.0	8	0.64	12.5	1.4	1.197	4.4	3.896	$3.327 \times 10^6$	3.59	8	0.88
II	1.0	4	.64	6.25	1.0	.855	4.4	3.896	3.327	3.59	12	1.36
III	1.0	2	.64	3.13	.5	.4275	4.4	3.896	3.327	3.59	26	1.01
IV	1.0	4	.91	4.40	.5	.369	4.4	3.896	3.327	2.53	10	1.22

TABLE II.- COMPARISON OF STRUT PENETRATION  
WITH FLAT-PLATE PENETRATION

Configuration	$q_r$		P/d	
	Strut	Flat plate (ref. 6)	Strut	Flat plate (ref. 6)
I	1.4	1.5	2.65	6.47
II	1.0	1.0	1.67	5.85
III	.5	.5	1.18	4.75
IV	.5	.5	1.18	4.53

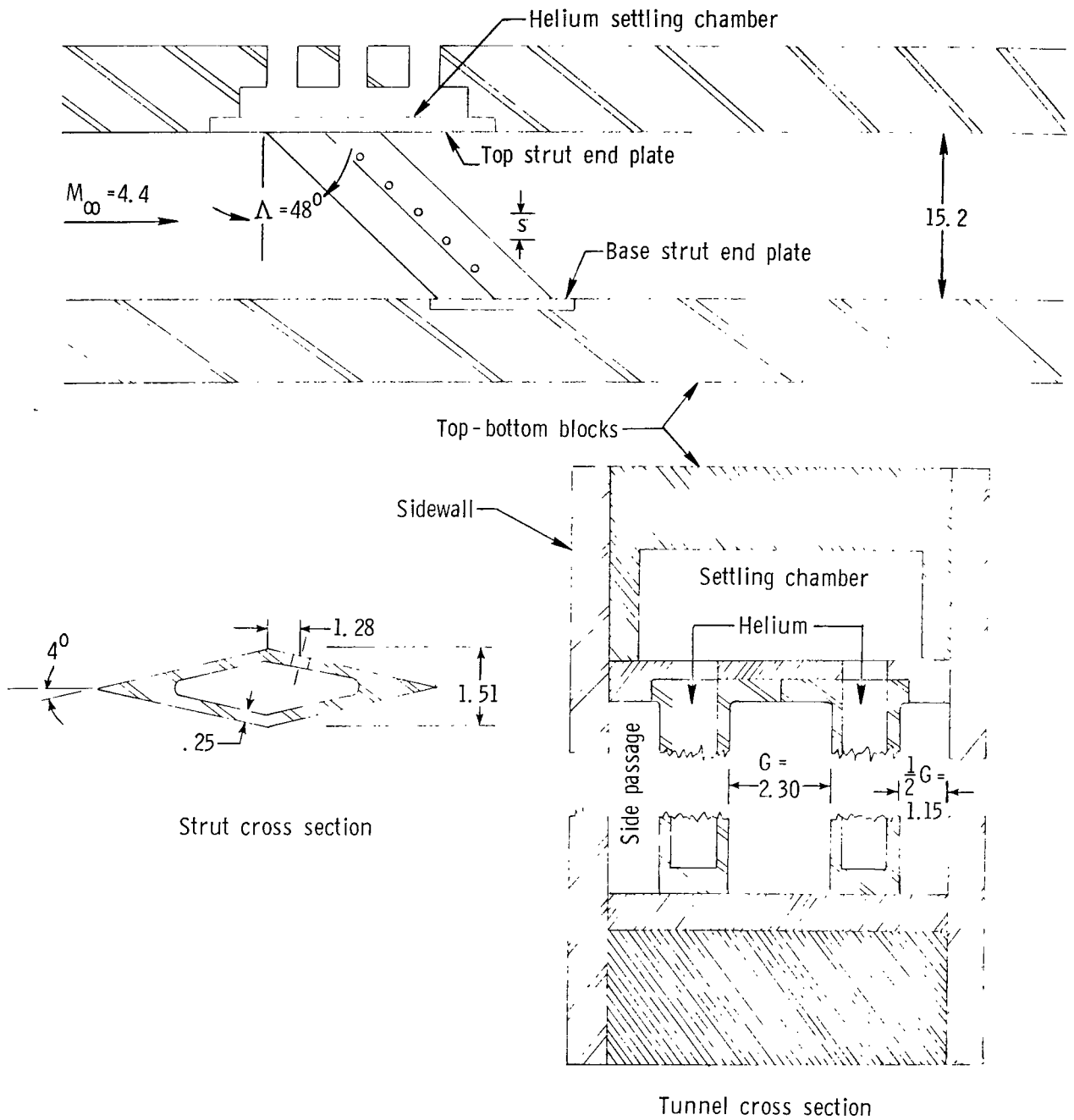
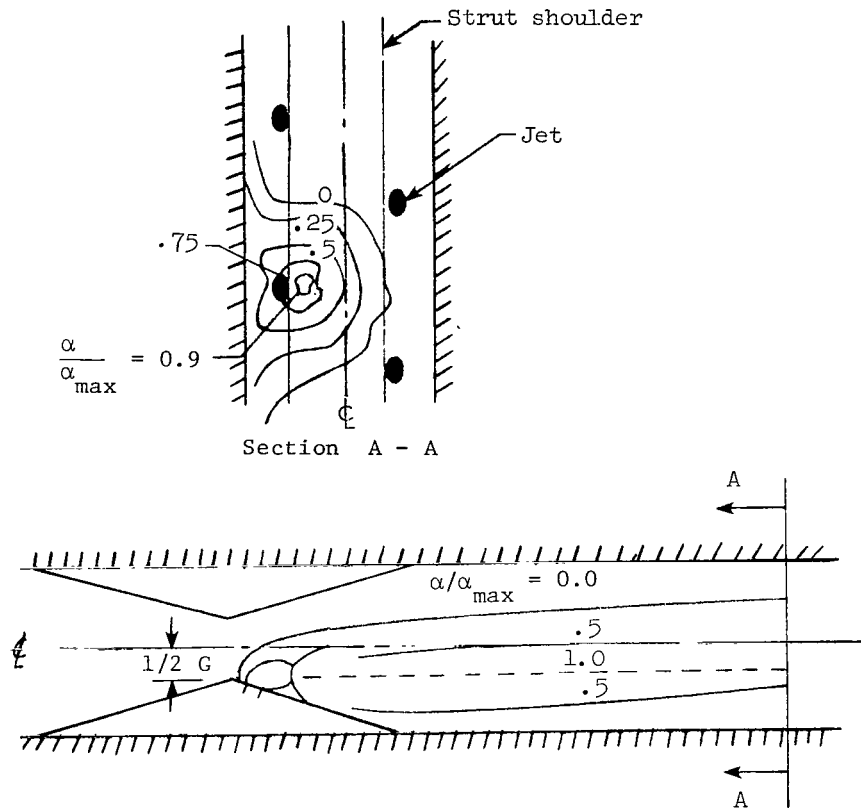
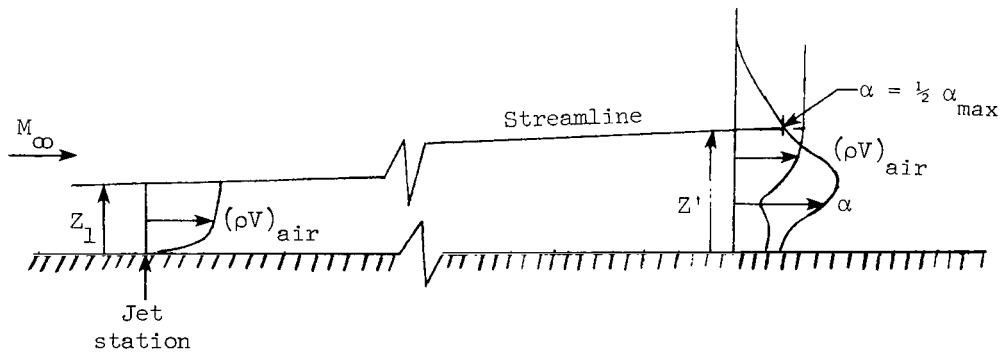


Figure 1.- Tunnel and strut details. All dimensions are in centimeters.



(a) Swept-strut flow model using flat-plate data.



(b) Flat-plate model

Figure 2.- Jet diameter selection. Contours from reference 6 using hydrogen injection.

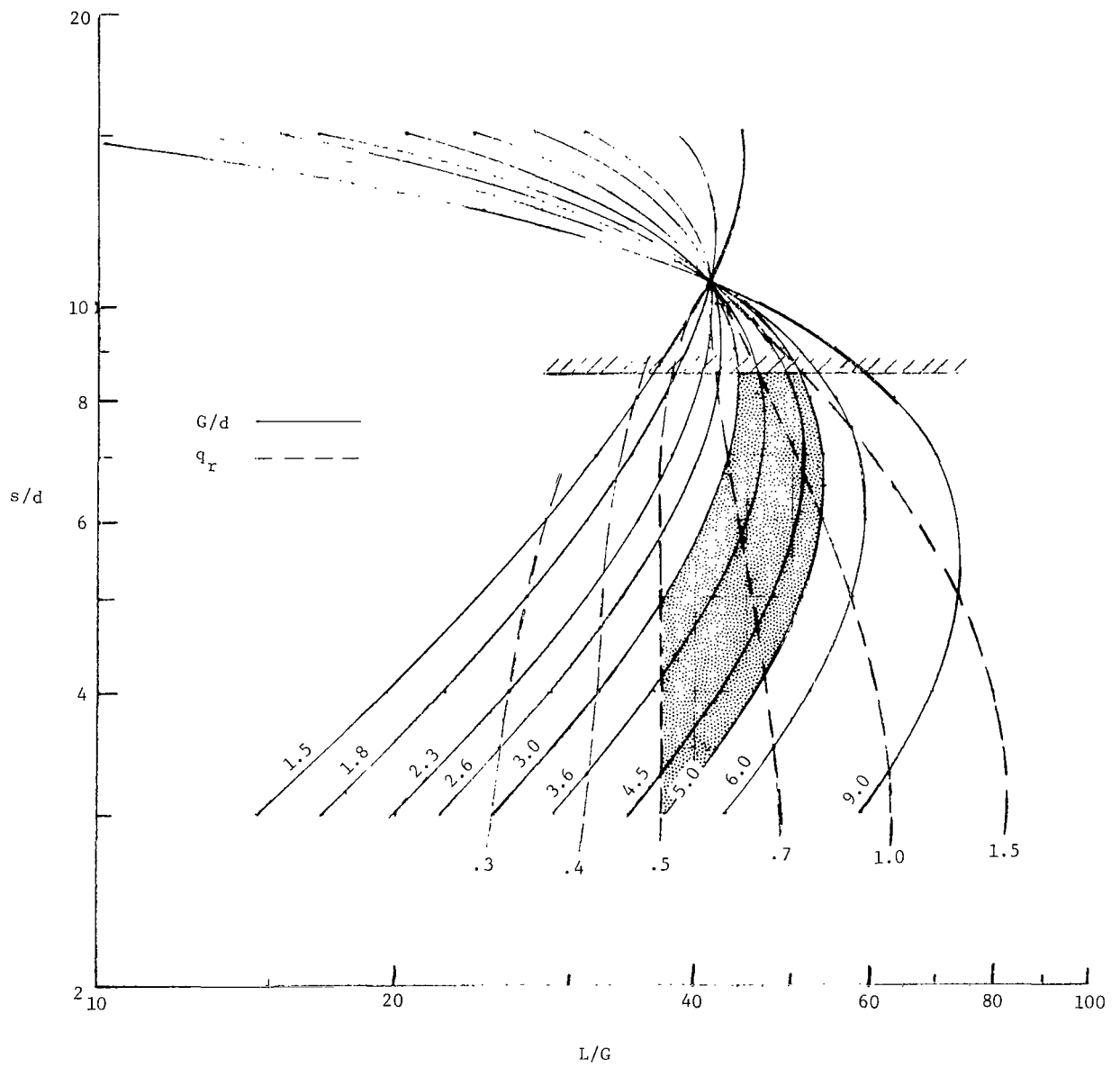
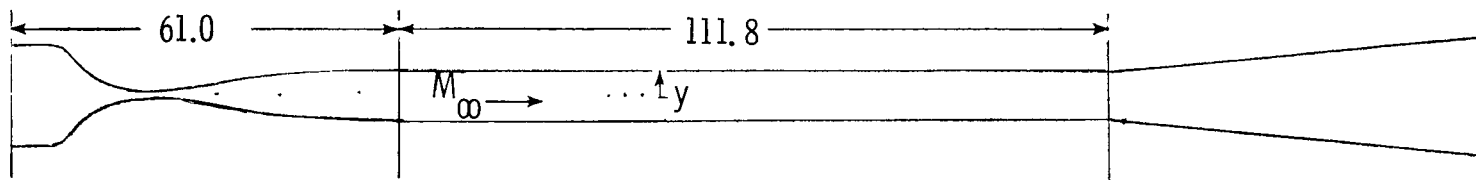
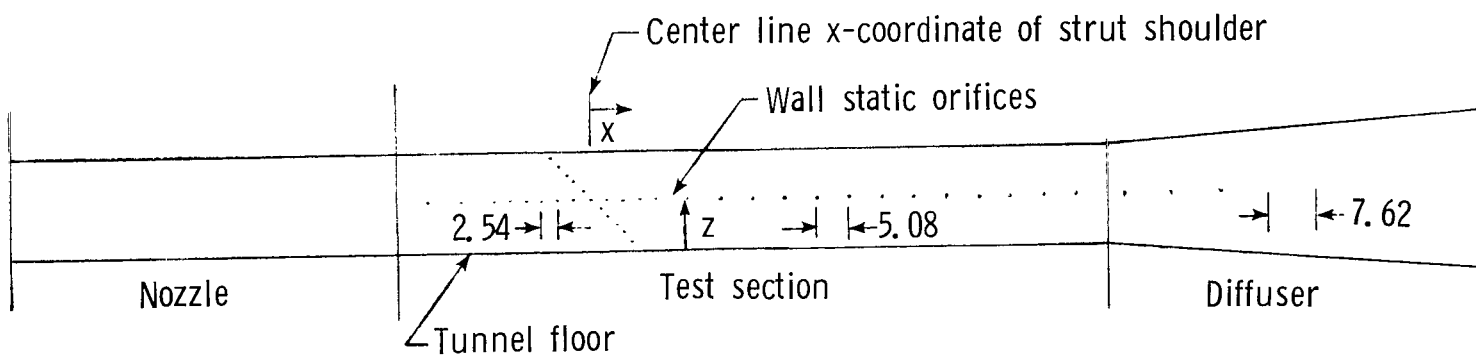


Figure 3.- Predicted mixing length to  $\eta_m = 0.95$ .



(a) Top view.



(b) Side view.

Figure 4.- Location of tunnel-wall static orifices. All dimensions are in centimeters.

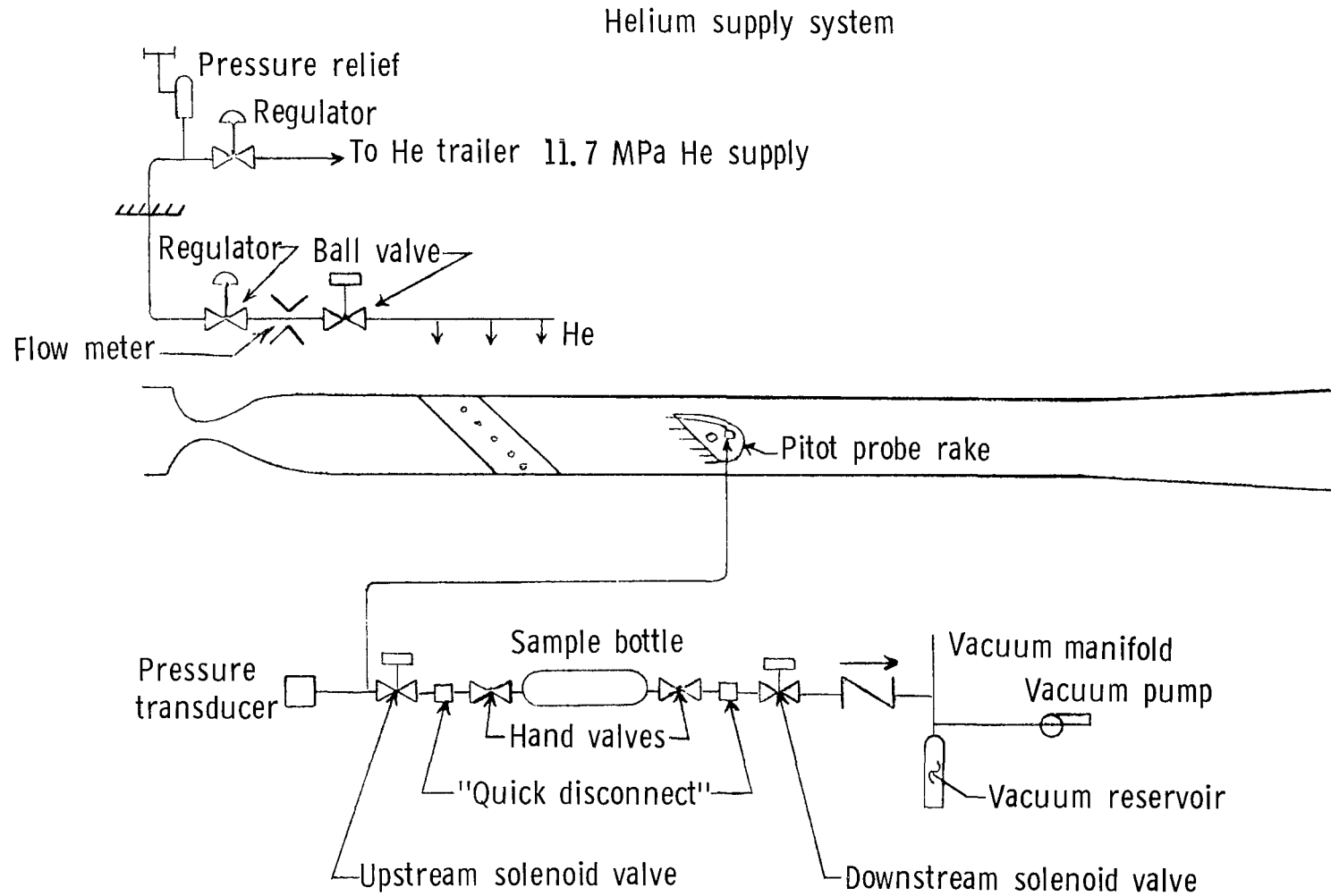


Figure 5.- Systems.



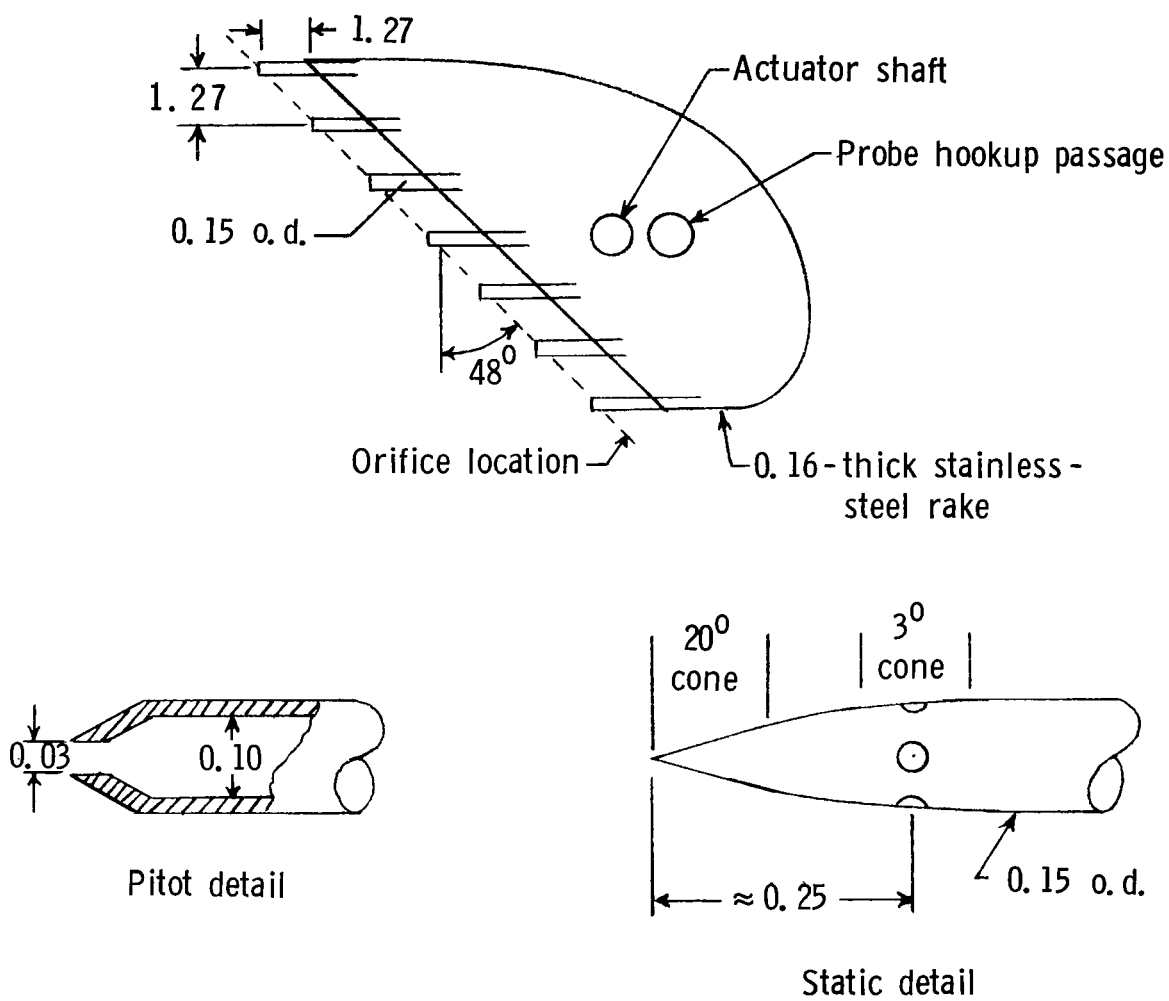


Figure 6.- Probe rake and details. All dimensions are in centimeters.

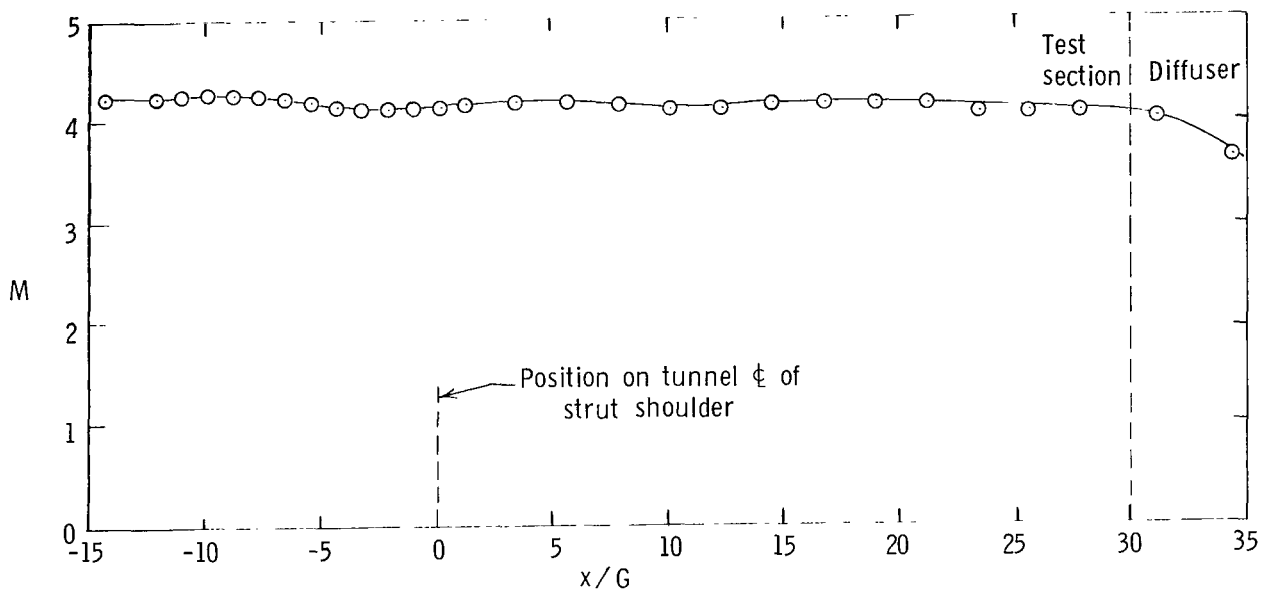


Figure 7.- Tunnel-wall Mach number based on  $p_w/p_{t,\infty}$ ;  $p_{t,\infty} = 3.861$  MPa.

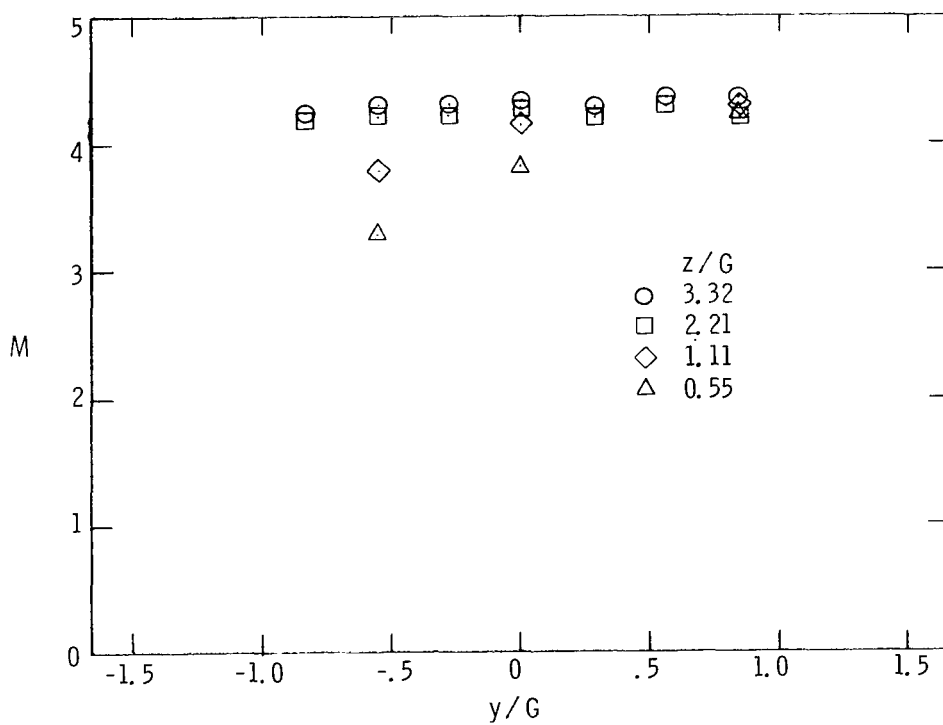


Figure 8.- Mach number profiles; no struts;  $x/G = 1.91$ .

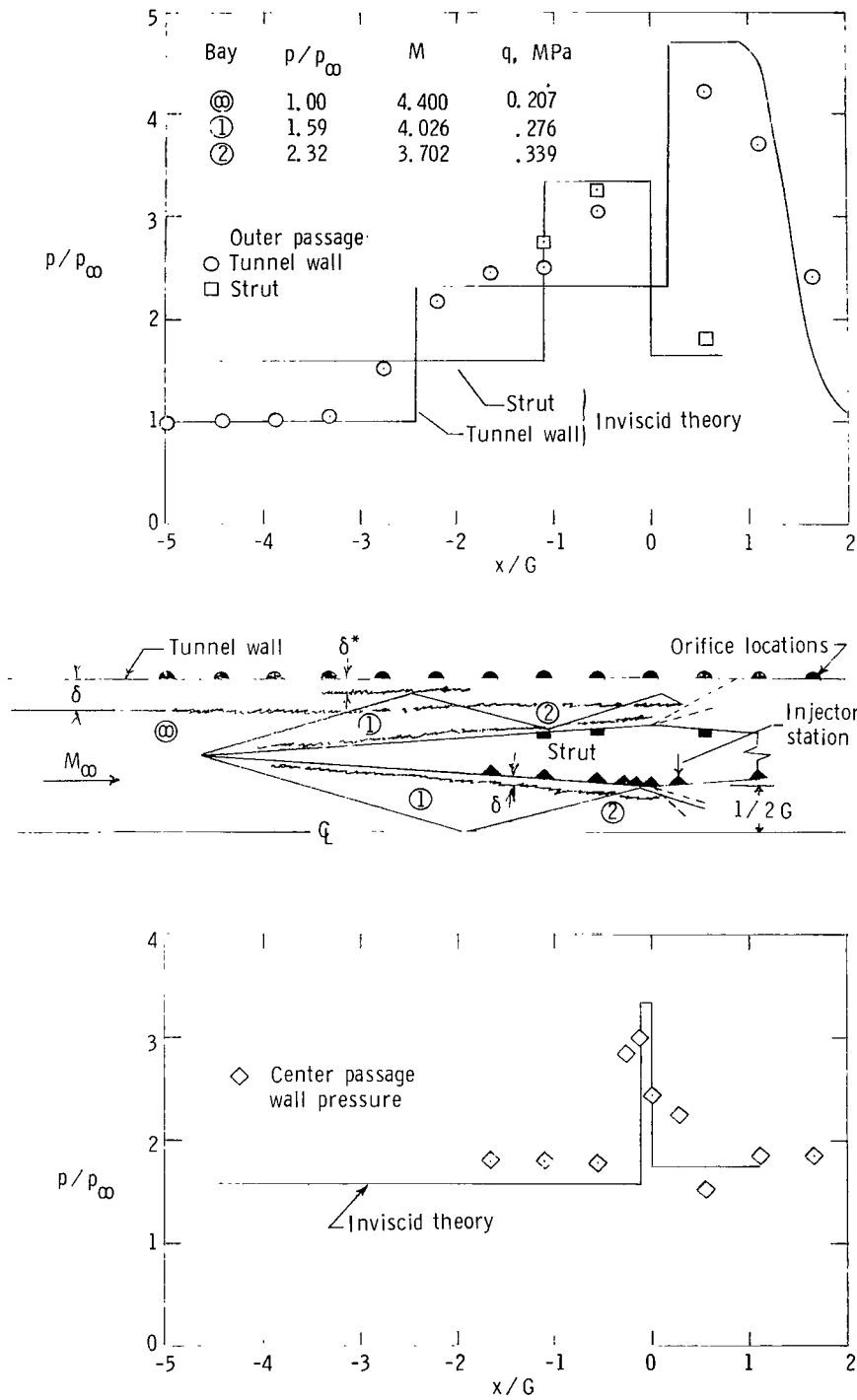
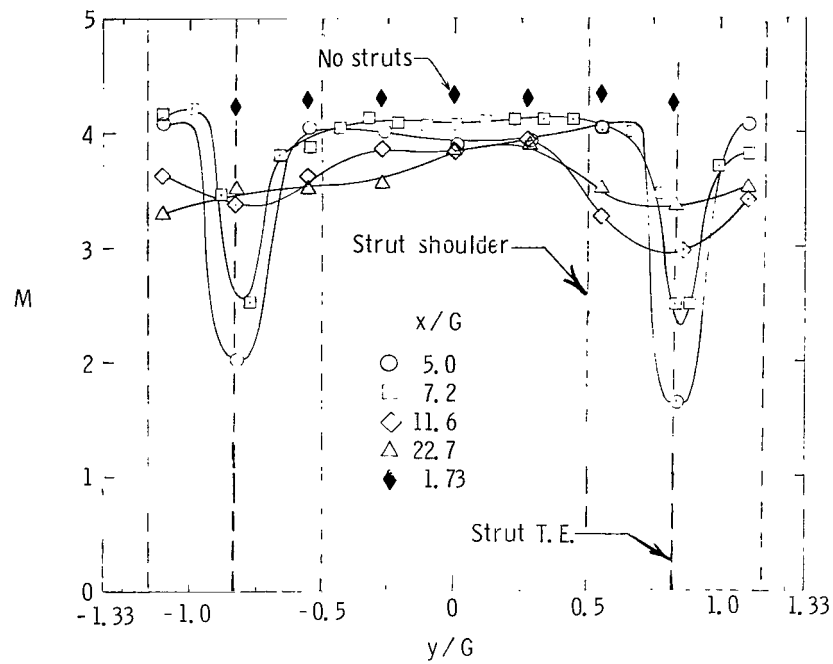
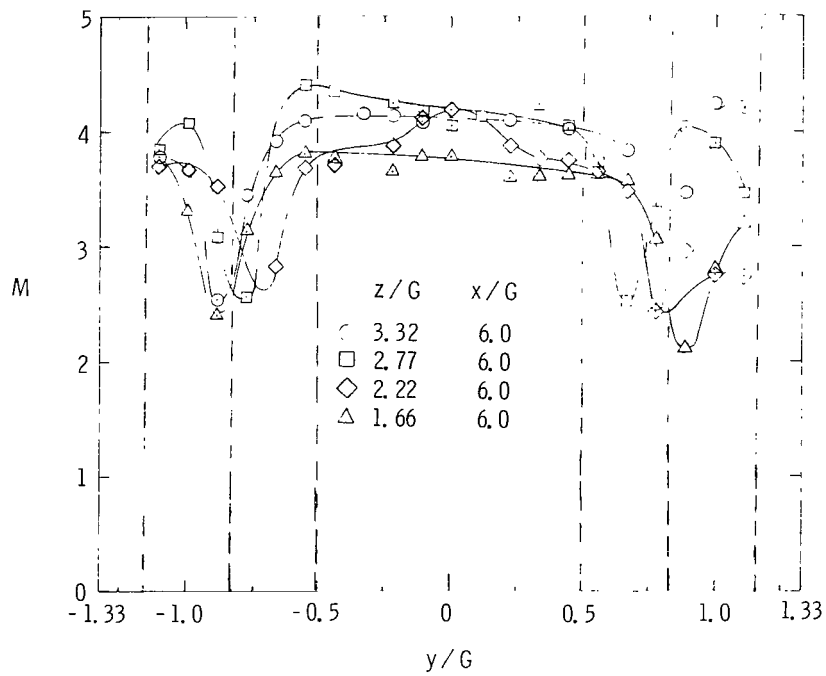


Figure 9.- Predicted strut flow and measured wall statics.



(a) Variation with downstream distance;  $z/G = 3.32$ .



(b) Strut end effects.

Figure 10.- Mach number surveys; no injection.

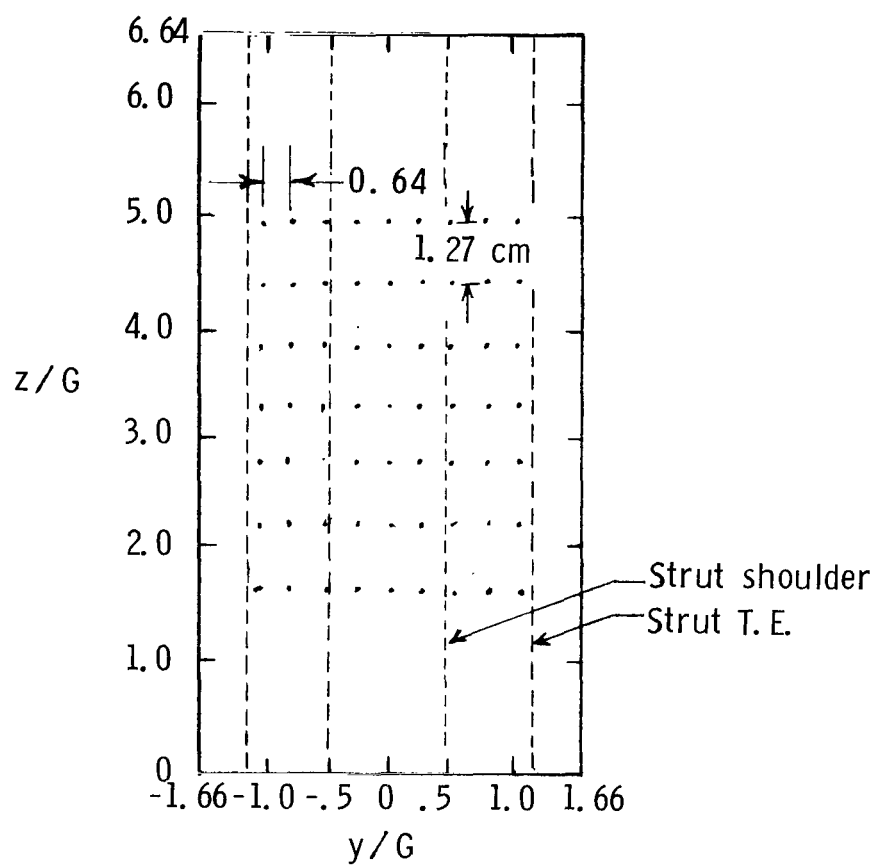
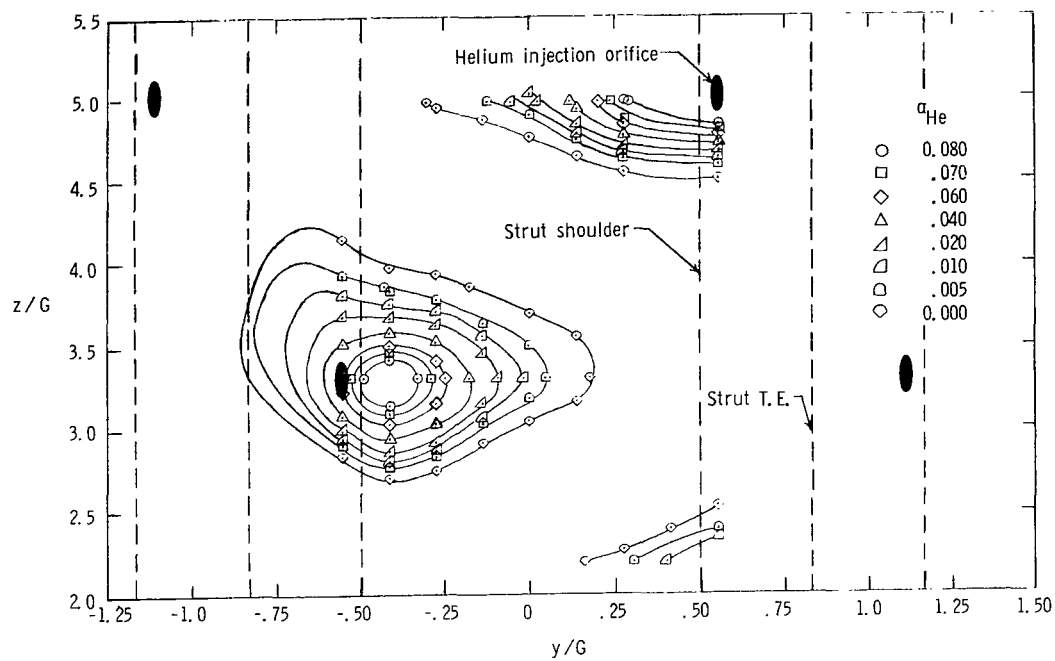
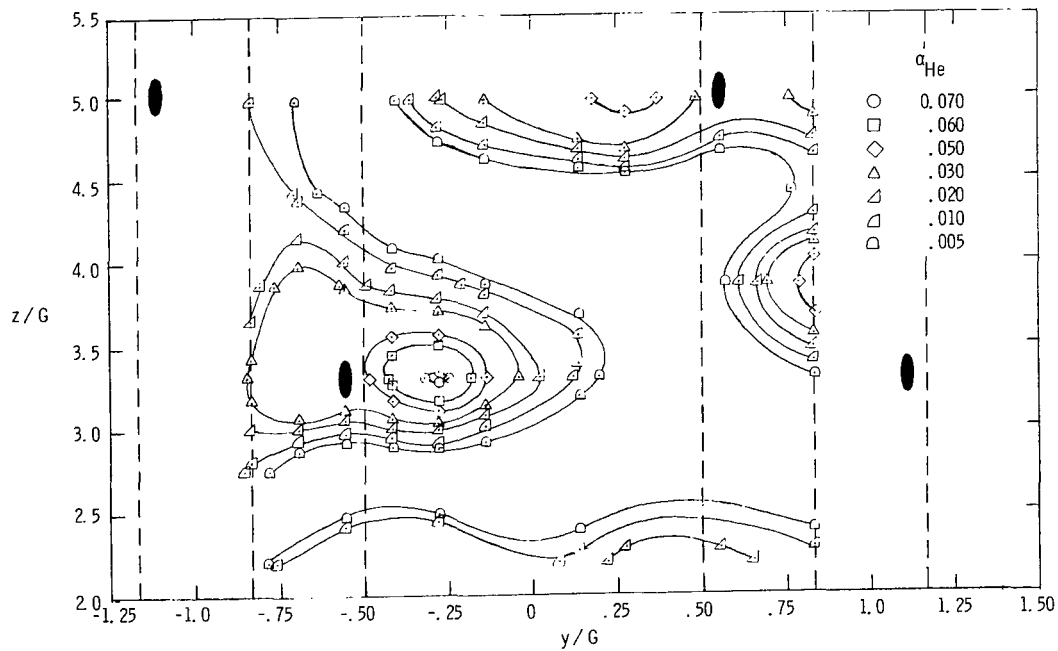


Figure 11.- Minimum data point grid (tunnel cross section).

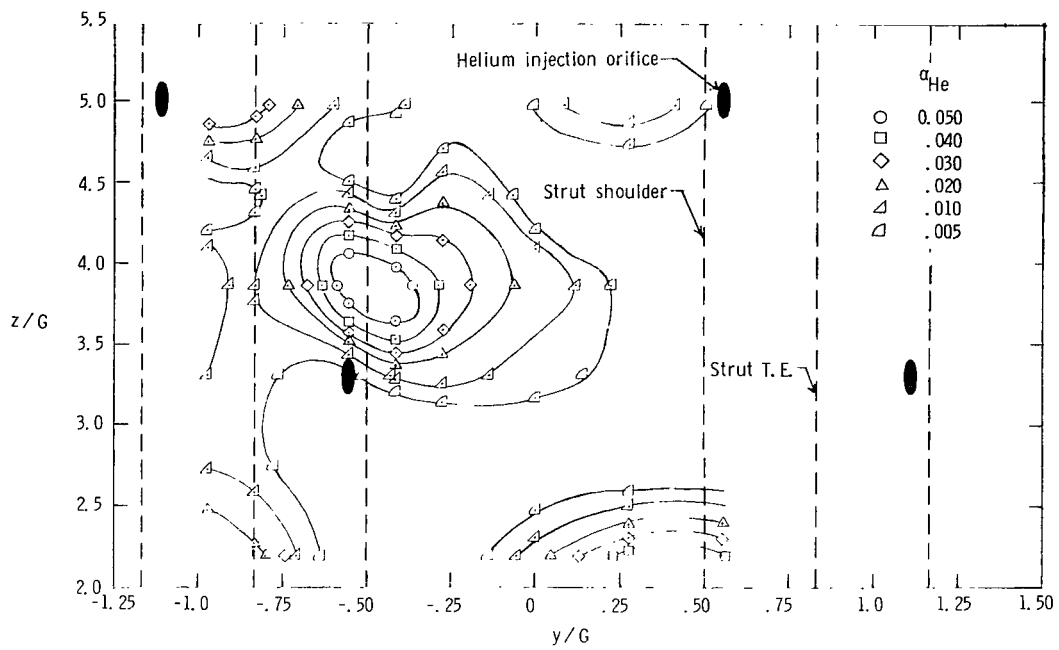


(a)  $x/G = 5.0$ .

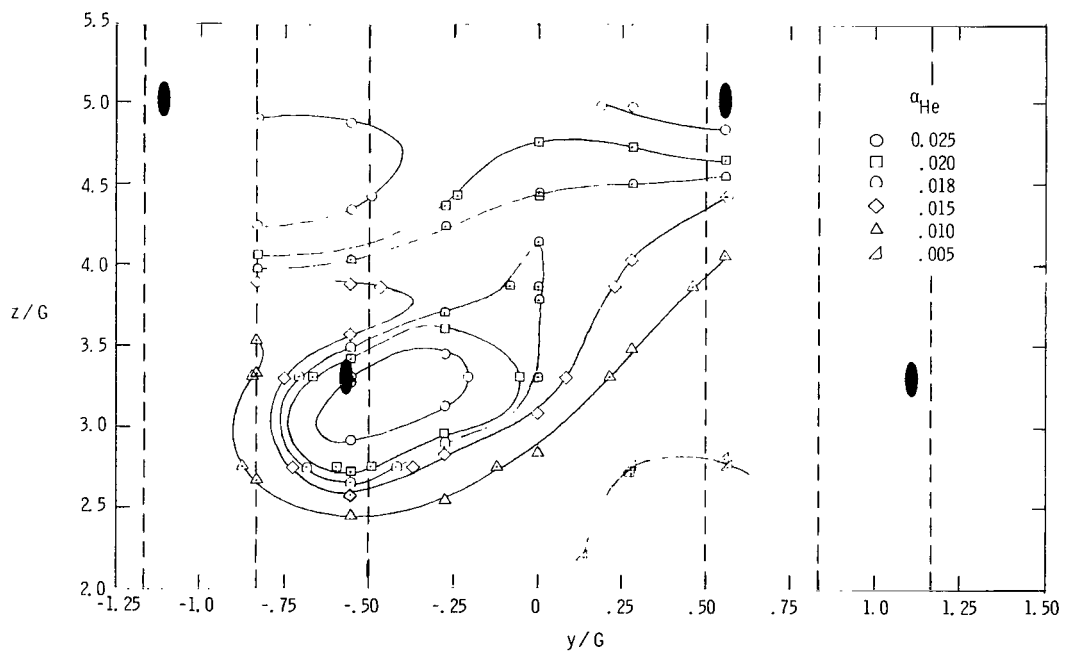


(b)  $x/G = 7.2$ .

Figure 12.- Helium mass concentration contour for configuration I.

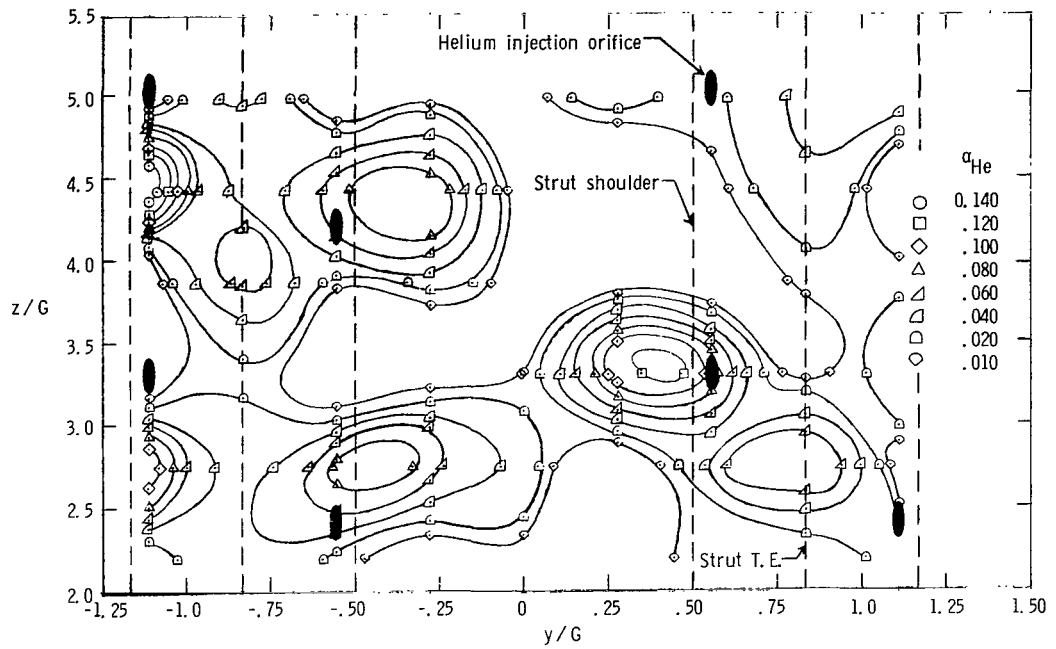


(c)  $x/G = 11.6$ .

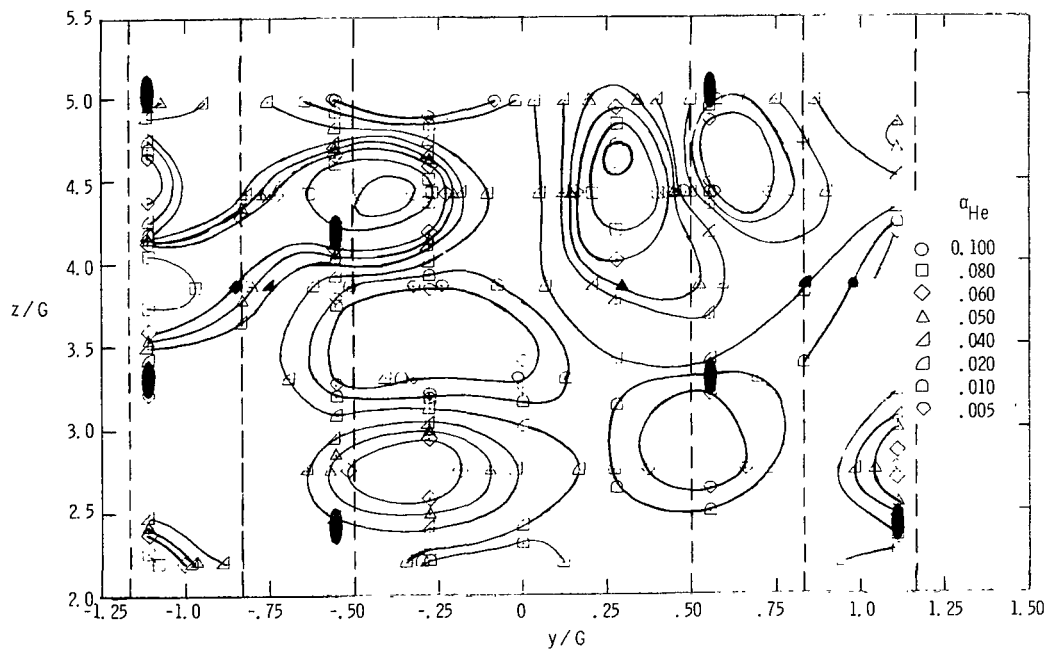


(d)  $x/G = 22.7$ .

Figure 12.- Concluded.



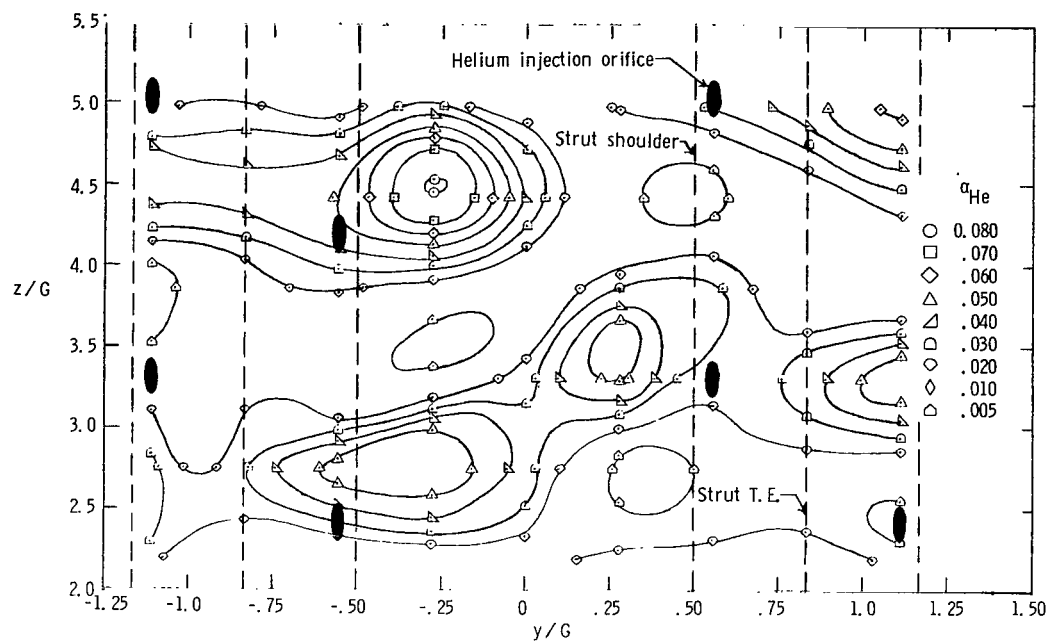
(a)  $x/G = 5.0$ .



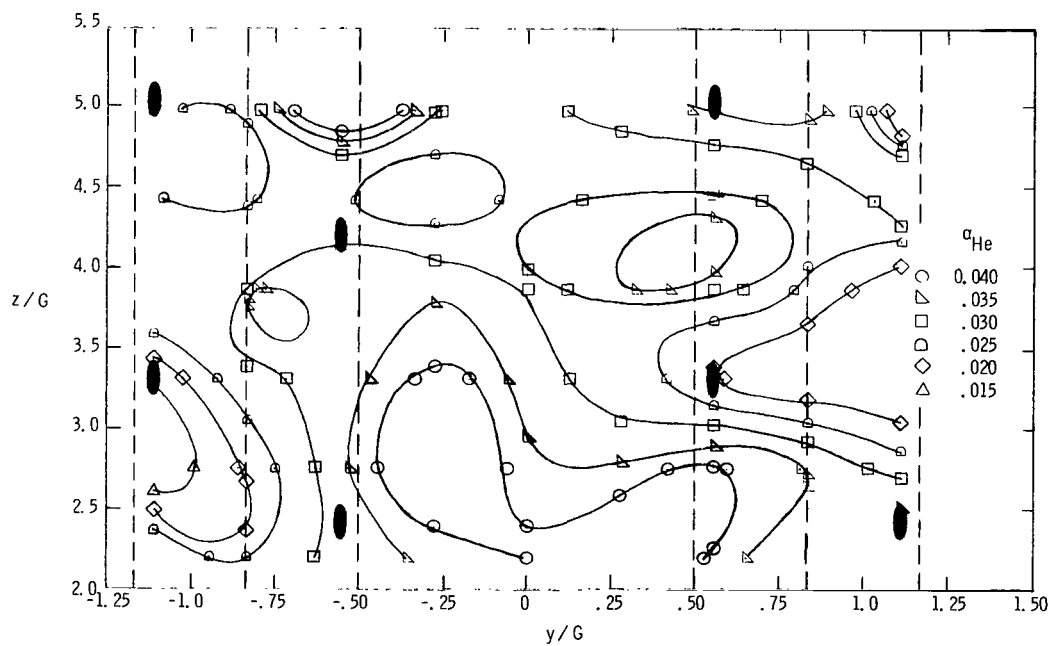
(b)  $x/G = 7.2$ .

Figure 13.- Helium mass concentration contour for configuration II.



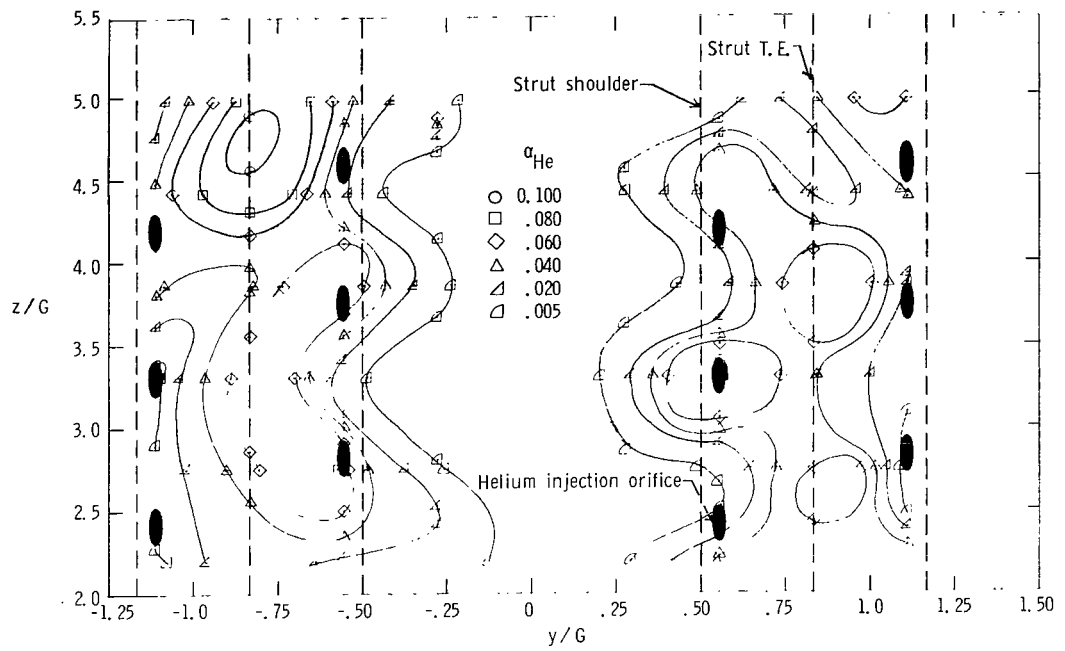


(c)  $x/G = 11.6$ .

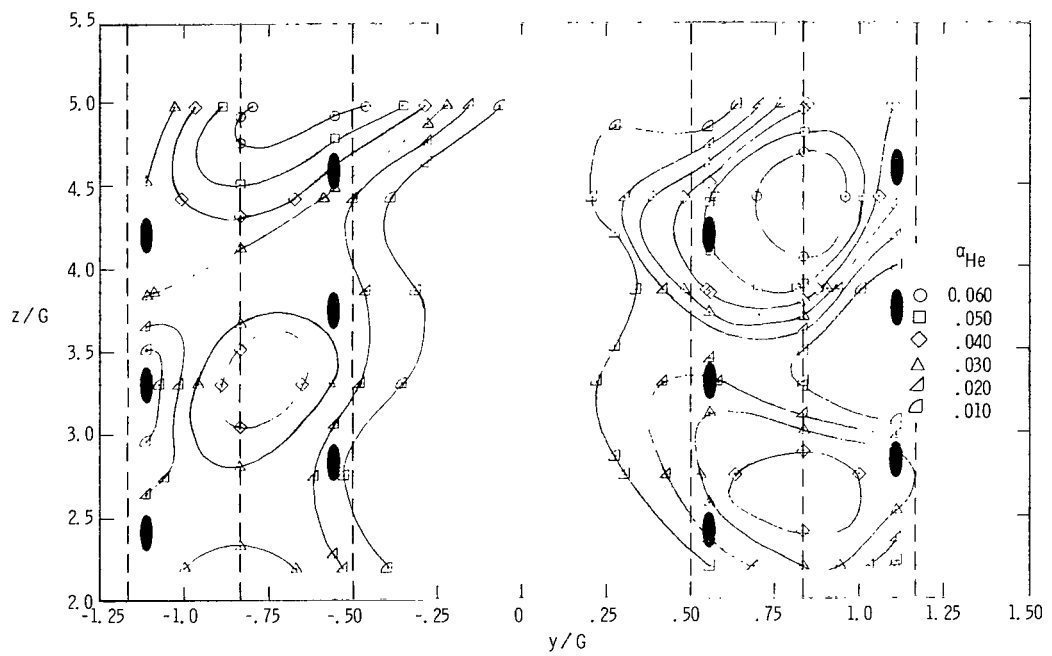


(d)  $x/G = 22.7$ .

Figure 13.- Concluded.

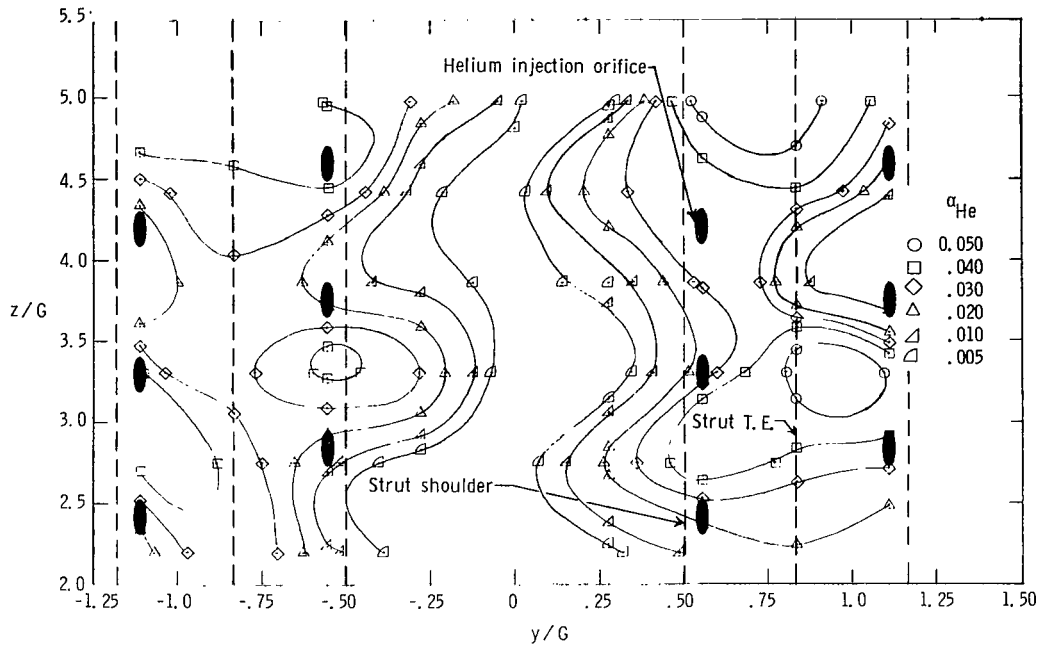


(a)  $x/G = 5.0$ .

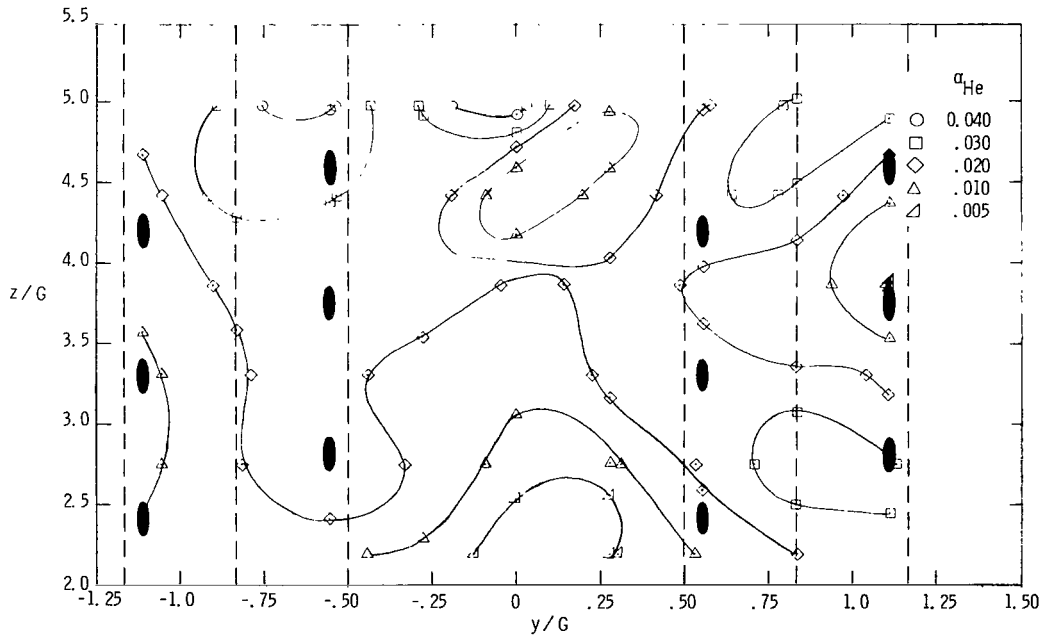


(b)  $x/G = 7.2$ .

Figure 14.- Helium mass concentration contour for configuration III.

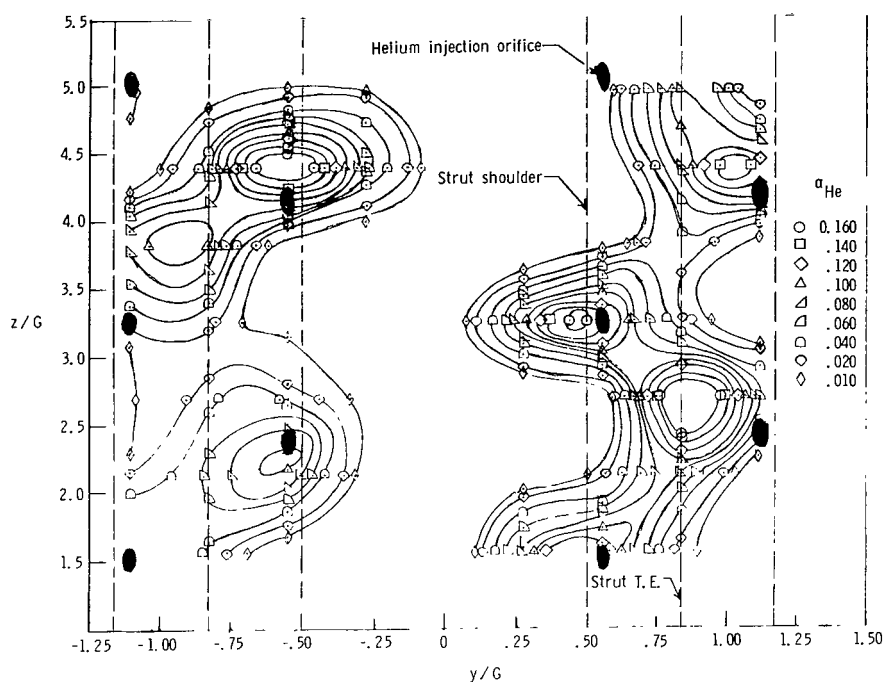


(c)  $x/G = 11.6$ .

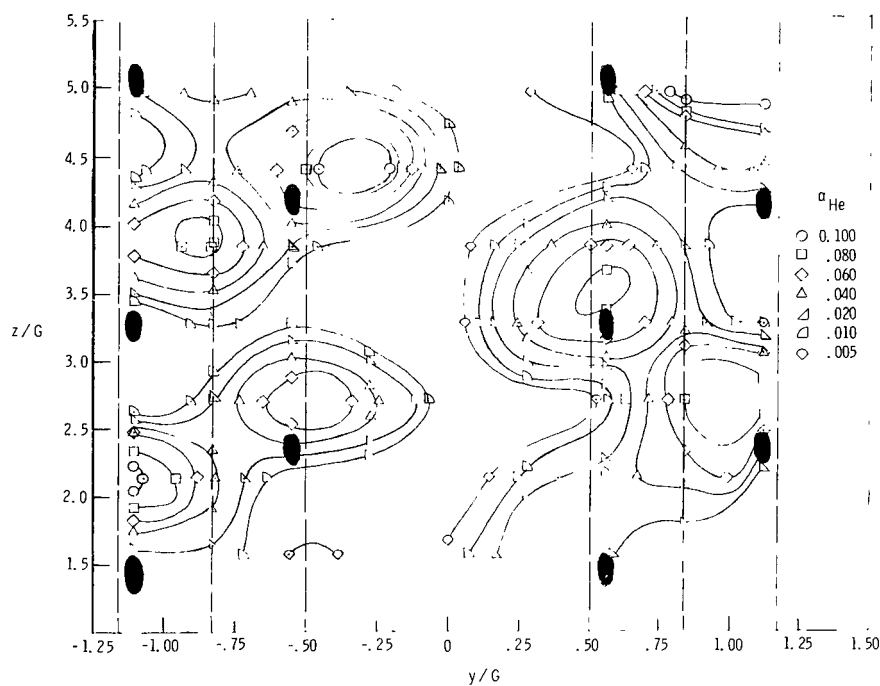


(d)  $x/G = 22.7$ .

Figure 14.- Concluded.

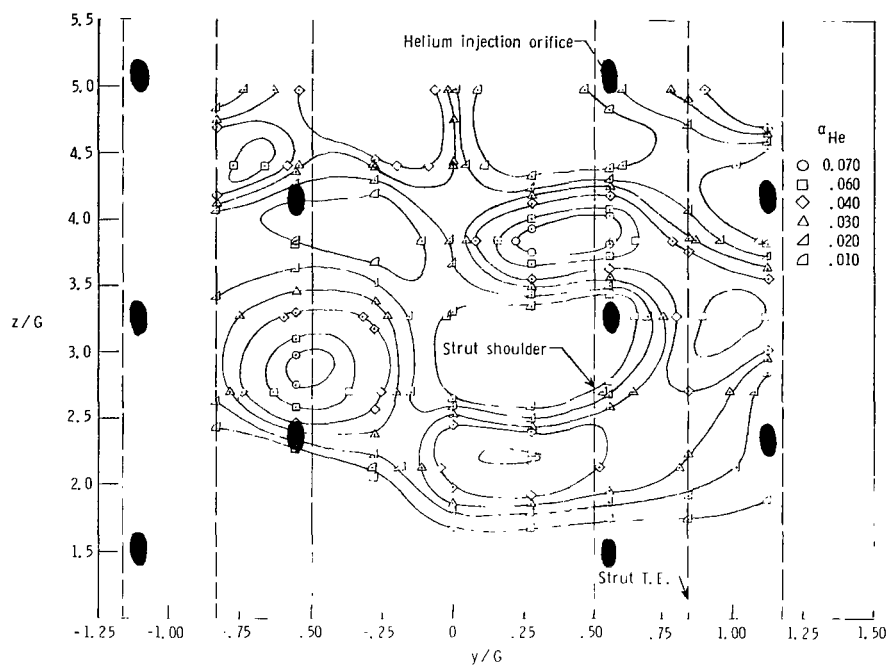


(a)  $x/G = 5.0$ .

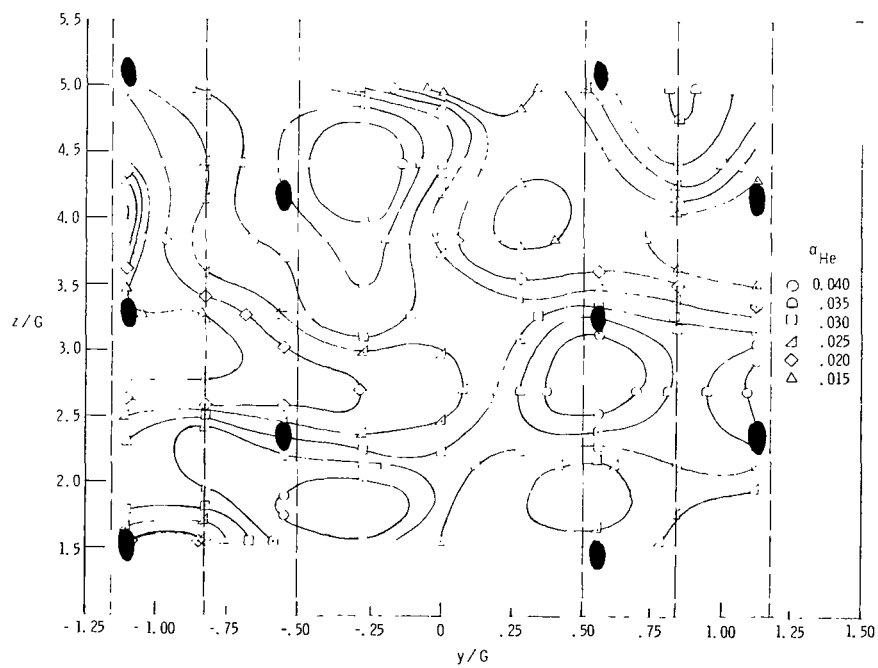


(b)  $x/G = 7.2$ .

Figure 15.- Helium mass concentration contour for configuration IV.



(c)  $x/G = 11.6$ .



(d)  $x/G = 22.7$ .

Figure 15.- Concluded.

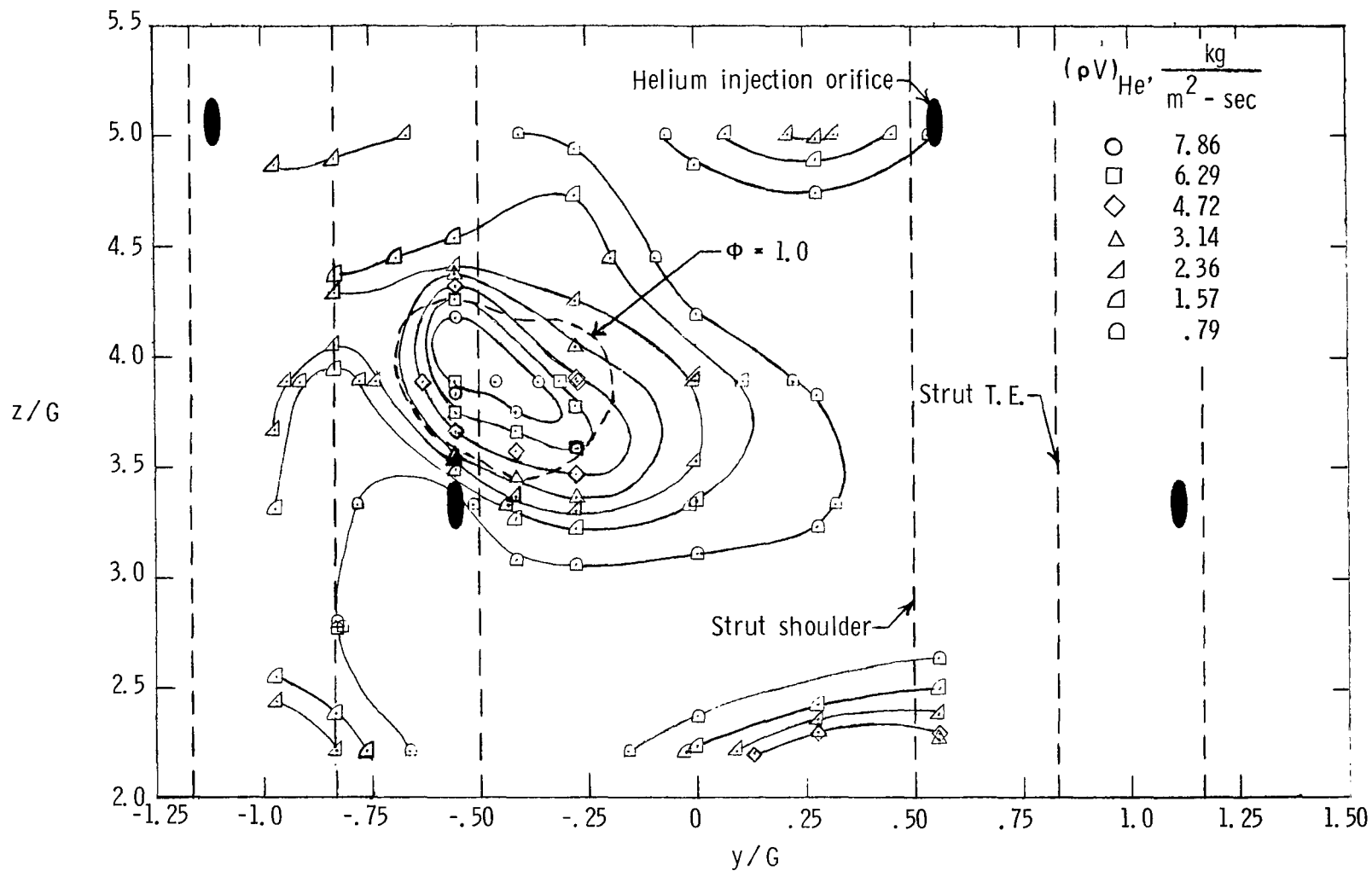


Figure 16.- Sample helium mass-flow contour. Configuration I;  $x/G = 11.6$ .

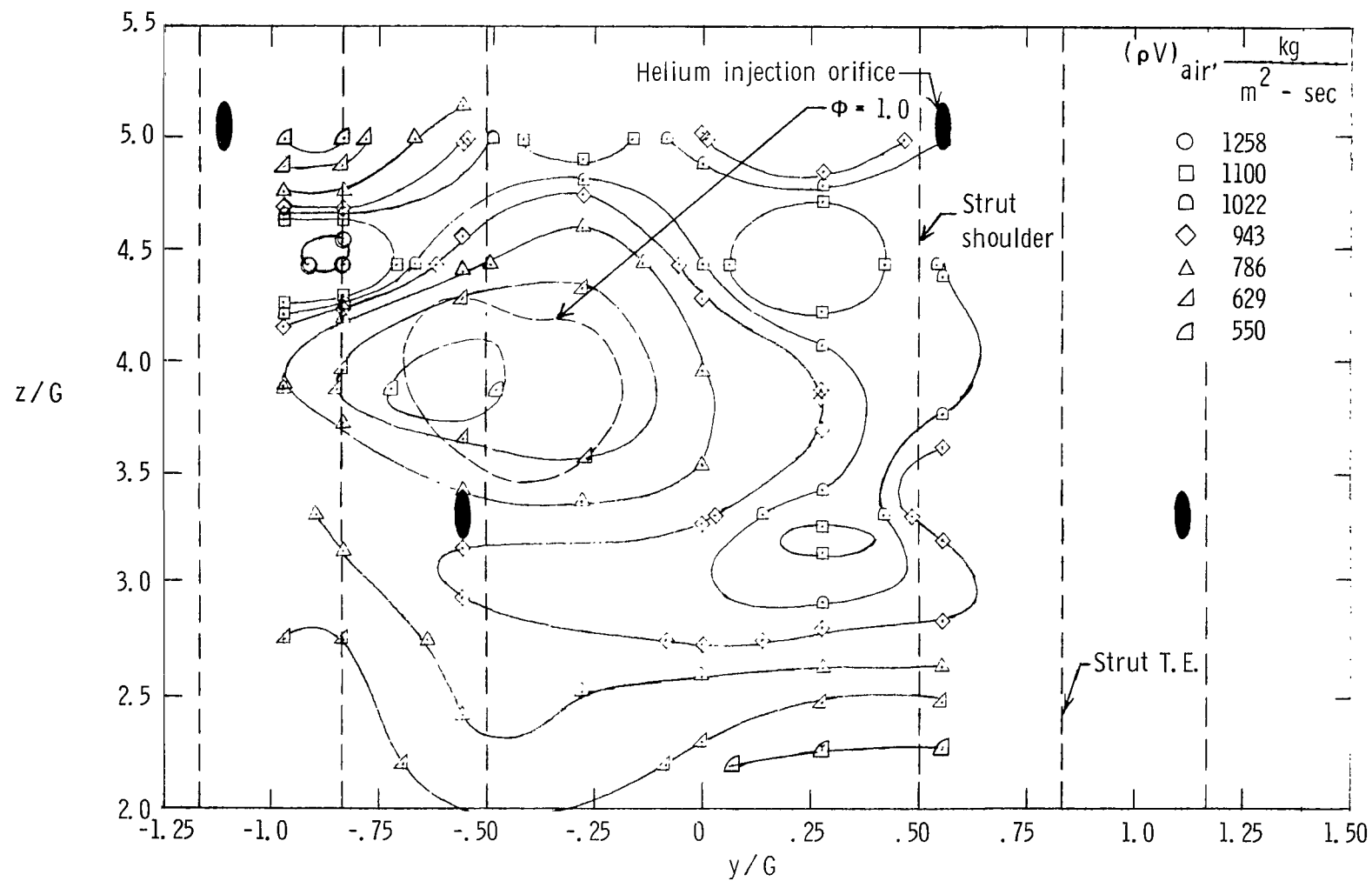


Figure 17.- Sample air mass-flow contour. Configuration I;  $x/G = 11.6$ .

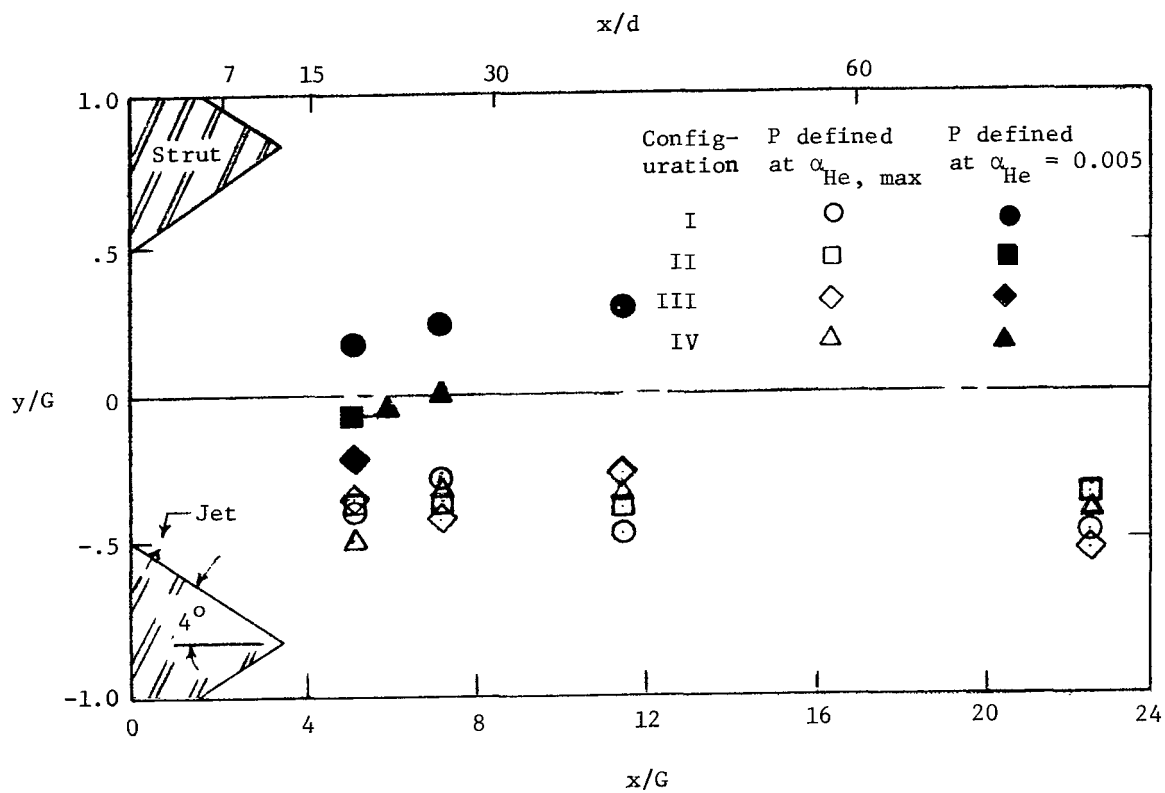
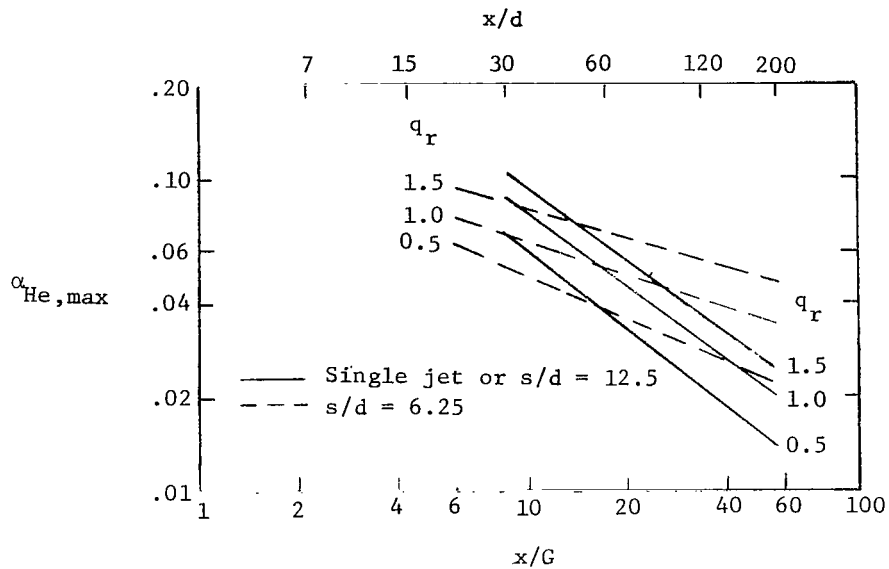
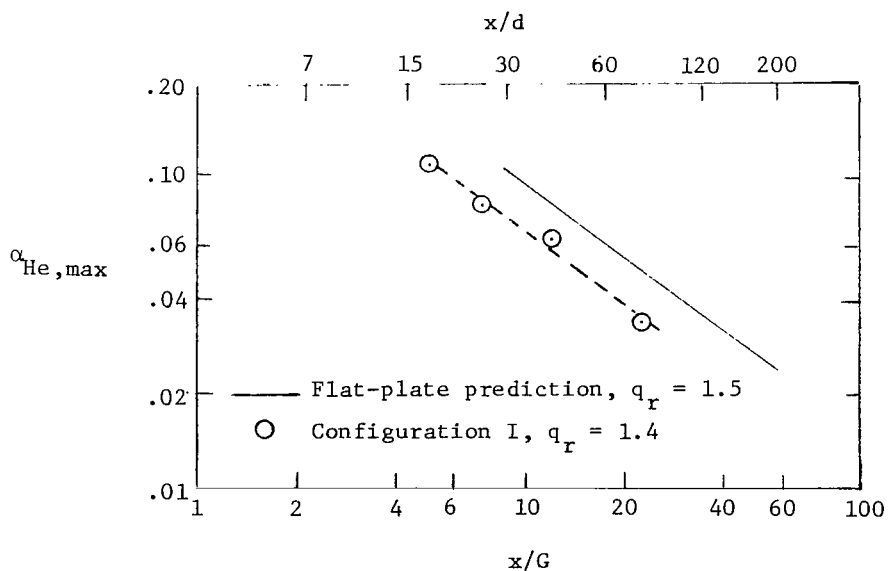


Figure 18.- Helium penetration.



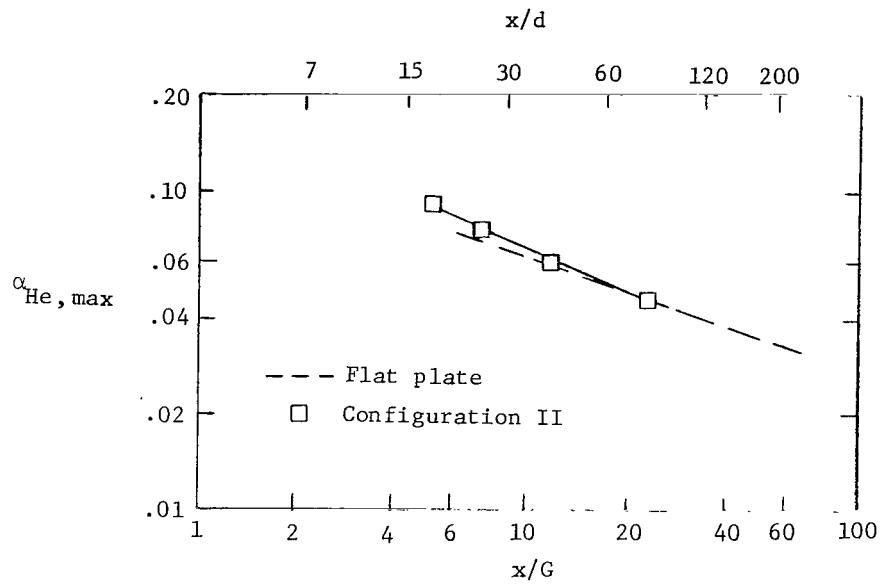


(a) Flat-plate results from references 6 and 7.

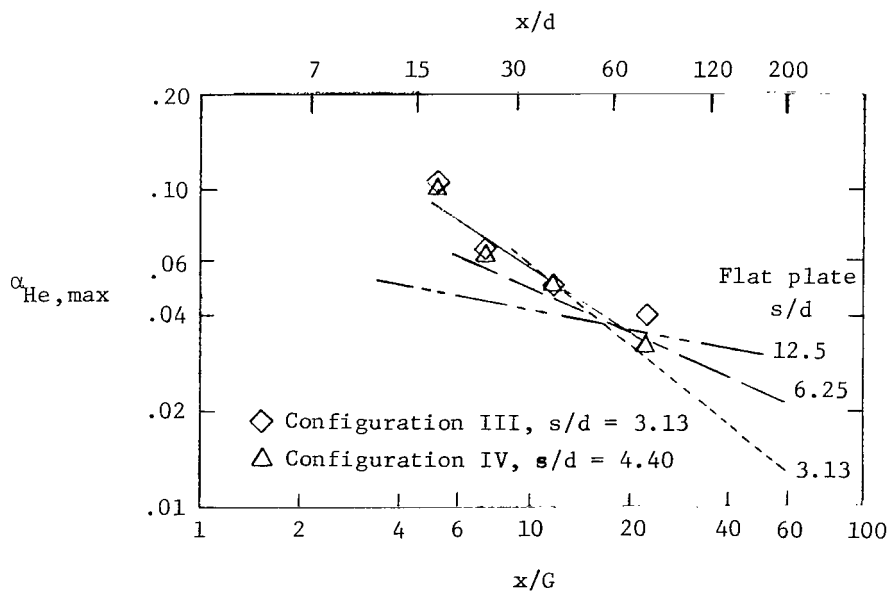


(b) Comparison of configuration I data with flat-plate data from reference 7;  $s/d = 12.5$ .

Figure 19.- Decay of maximum concentration.

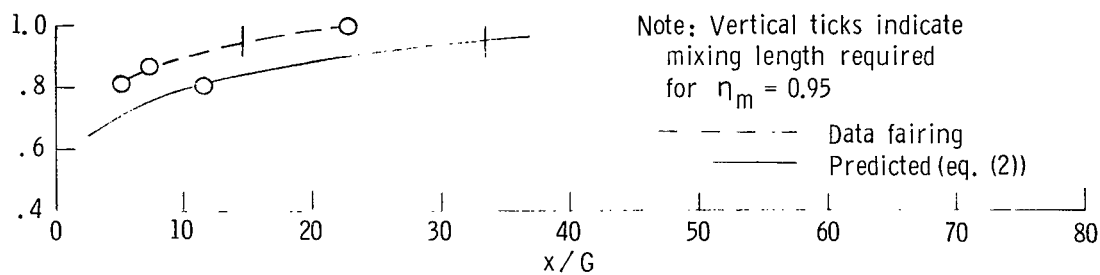


(c) Comparison of configuration II data with flat-plate data from reference 7;  $s/d = 6.25$ ;  $q_r = 1.0$ .

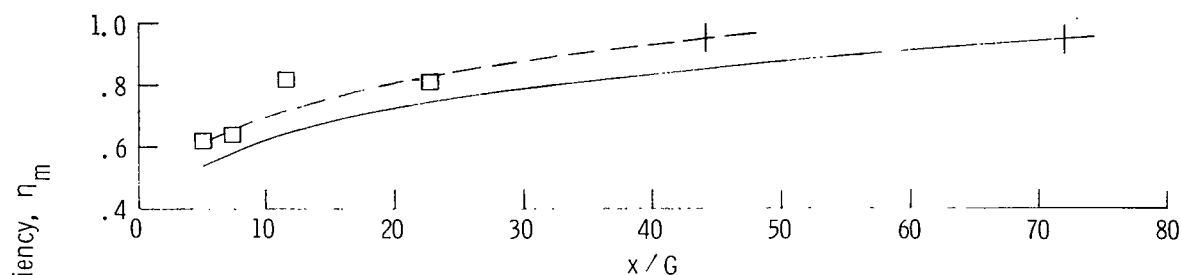


(d) Comparison of configurations III and IV data with flat-plate data from reference 7;  $q_r = 0.5$ .

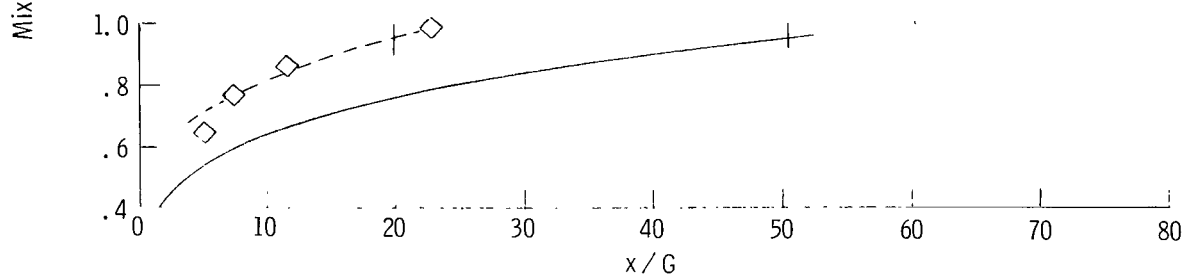
Figure 19.- Concluded.



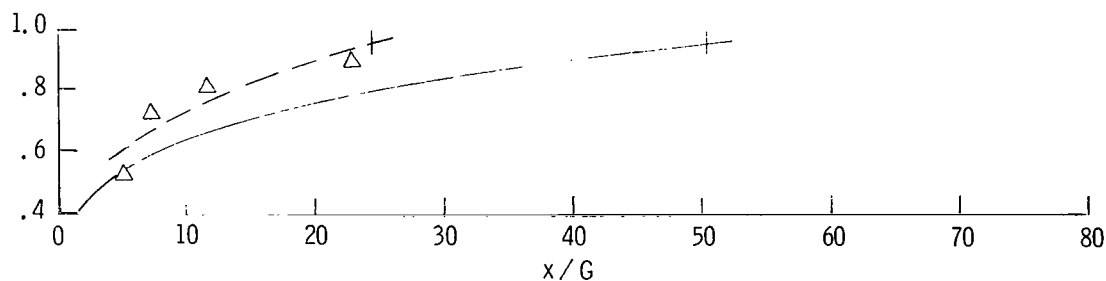
(a) Configuration I;  $s/d = 12.5$ ;  $q_r = 1.4$ ;  $\phi = 0.88$ .



(b) Configuration II;  $s/d = 6.25$ ;  $q_r = 1.0$ ;  $\phi = 1.36$ .



(c) Configuration III;  $s/d = 3.13$ ;  $q_r = 0.5$ ;  $\phi = 1.01$ .



(d) Configuration IV;  $s/d = 4.40$ ;  $q_r = 0.5$ ;  $\phi = 1.22$ .

Figure 20.- Measured and predicted mixing lengths.